ARTICLE OPEN

Check for updates

The axon initial segment-associated microglia regulate neuronal activity and visual perception

Yaping Wang[1,3], Qiushi Wang[1,3], Chen Gao[1], Shu He[1], Cheng Wei[1], Jia Song[1], Xinli Liu[2], Xiaoli Liu[1], Shi Feng[1], Wen Yao[1], Wen Wu[2], Tian-Ming Gao[1] and Siqiang Ren[1,2]✉

As innate immune cells in the brain, microglia directly contact excitatory neurons and regulate their activities under various conditions; however, the mechanisms of direct microglia–neuron functional interactions remain largely unknown. Here, we identified one special population of neocortical microglia that specifically associate with the axon initial segments (AISs) of excitatory neurons, and could regulate their activities and contribute to visual perception. We found that brief depolarization of AIS-associated microglia, but not the AIS-non-associated microglia, significantly promoted the action potential firing of related excitatory neurons, which relied mechanistically on microglial K^+ release through the outward K^+ channel THIK-1. Interestingly, in vivo visual stimulation with drifting gratings evoked microglial transient depolarizations specifically on the processes, which depended on muscarinic receptors and triggered K^+ release through THIK-1; meanwhile, visual stimulation induced more robust calcium responses in neurons associated with microglia at their AISs compared with nearby unassociated neurons. Disruption of the AIS–microglia interaction disturbed calcium responses specifically in neurons associated with microglia at their AISs, impaired the coordinated activity of the entire neural ensemble, and thereby affected the visual discrimination behavior of awake mice. Collectively, our findings identified a new type of microglia–neuron functional interaction that may be critical for higher-order brain functions.

Cell Research (2026) 36:249–271; https://doi.org/10.1038/s41422-026-01218-8

INTRODUCTION

The mammalian brain is composed of diverse cell types with different morphological and functional properties that collaboratively orchestrate various brain functions.[1,2] Among these cells, neurons can form densely connected networks for signal transmission and processing, which is essential for cognitive functions,[3,4] whereas glial cells, including astrocytes, microglia (MGs), and oligodendrocytes, cooperatively support and modulate neuronal functions.[5–9] For example, with processes located near the axon initial segment (AIS) and nodes of Ranvier of myelinated axons in layer 5 and white matter of the rodent neocortex, astrocytes can directly regulate neuronal excitability and action potential (AP) propagation, thus controlling information flow and neural circuit function.[10]

As innate immune cells in the central nervous system (CNS), MGs dynamically patrol the brain environment and elaborately regulate neurogenesis, synapse formation, neural circuit wiring, and neuronal activities under various physiological or pathological conditions.[8,11–14] It is well established that MGs can directly and indirectly interact with excitatory pyramidal neurons (PNs) in the neocortex. Direct interactions between MGs and PNs, such as at the axonal boutons, dendritic spines, somata, and nodes of Ranvier, enable more precise and effective modulation of diverse neuronal functions by MGs.[12,15–23] For example, direct interactions at the axonal boutons or dendritic spines enable MGs to induce synapse formation[18] and prune redundantly formed synapses[22] during early development, and remodel neural circuits at the adult stage,[16,17] and even mediate synapse loss in neurodegenerative diseases.[20] A recent study also suggests that MGs can form specialized purinergic junctions with neuronal somata to protect against hyperexcitation or excitotoxicity in neurodegenerative disorders such as stroke.[24] Interestingly, several recent studies have identified the neuronal AISs as a new location for direct MG–PN interactions.[25–27] Notably, the AIS–MG interaction can be disrupted when MGs are activated in neuroinflammatory conditions, suggesting that this interaction may play more active roles in normal brain functions.[25] Indeed, one recent study showed that this MG interaction regulates inhibitory axo-axonic synaptogenesis onto the AISs from chandelier cells during early postnatal development.[26] However, the physiological functions of the AIS–MG interaction are largely unknown.

The AIS is a 20–60-μm long compartment located at the proximal axon/soma interface that is enriched in voltage-gated ion channels, membrane proteins, and sub-membranous

[1]Guangdong-Hong Kong-Macao Greater Bay Area Center for Brain Science and Brain-Inspired Intelligence; State Key Laboratory of Multi-organ Injury Prevention and Treatment; Key Laboratory of Mental Health of the Ministry of Education; Guangdong Province Key Laboratory of Psychiatric Disorders; Guangdong Basic Research Center of Excellence for Integrated Traditional and Western Medicine for Qingzhi Diseases; Guangdong-Hong Kong Joint Laboratory for Psychiatric Disorders; Department of Neurobiology, School of Basic Medical Sciences, Southern Medical University, Guangzhou, Guangdong, China. [2]Department of Rehabilitation, Zhujiang Hospital, Southern Medical University, Guangzhou, Guangdong, China. [3]These authors contributed equally: Yaping Wang, Qiushi Wang. ✉email: rensiqiang159@smu.edu.cn

Received: 25 September 2025 Accepted: 21 December 2025
Published online: 28 January 2026

cytoskeleton scaffolds.[28,29] The AIS summates inputs from thousands of synapses to trigger AP firing, and it is the major regulatory site of neuronal excitability. Previous reports suggest that AIS length, location, ion channel density, and even extracellular ion concentrations may be strictly regulated and have critical effects on AP firing.[28,30–32] However, whether MGs can regulate neuronal activity through direct interaction with AISs and contribute to higher-order perceptive or cognitive brain functions remains to be determined.

In this study, we identified the AIS-associated MGs (AISa-MGs) as a special population of homeostatic MGs that share some common morphological and transcriptomic features. Brief depolarization of AISa-MGs promoted AP firing of the associated PNs in the neocortex via release of K^+ through THIK-1 channels directly to the AISs. Interestingly, in vivo visual stimulation with drifting gratings evoked transient depolarizing events specifically on microglial processes rather than somata; these events were dependent on muscarinic receptors and subsequently triggered K^+ release through THIK-1 to restore microglial membrane potential (MP) to the resting level. Notably, a small proportion of PNs in layer 2/3 of the primary visual cortex (V1), which interacted with MGs at their AISs, responded more robustly to visual stimulation. Disruption of microglial depolarizing activity or THIK-1 function specifically disturbed the calcium responses of neurons associated with MGs at their AISs and significantly reduced the performance of awake mice in a visual discrimination task. These findings highlight a critical role for the direct AIS–MG functional interaction in the regulation of neuronal activity and higher-order brain functions.

RESULTS

A special subset of homeostatic MGs interact with neuronal AISs in the neocortex

We first visualized the physical contacts between MGs and AISs in the neocortex by immunostaining of the AIS marker AnkG in *Cx3cr1-Cre^{ERT};YFP* mice (Fig. 1a). Interestingly, each MG occupied a circled area and formed reiterated structures (Fig. 1a). We observed that a subset of MGs had a single primary or branch process (74.42% vs 25.58%) wrapping ~69.39% of the length of AISs (Fig. 1b–d), similar to previous reports.[25] The cell bodies of the AISa-MGs with primary processes wrapping AISs could also contact the AISs at the start, middle, or end region (~60.47%, 2.32%, and 11.63%, respectively) (Fig. 1c). Overall, there were ~21.03% MGs interacting with neuronal AISs (Fig. 1e), and most of the AISa-MGs interacted with only one AIS (Fig. 1f). Conversely, there were ~4.88% AISs interacting with MGs (Fig. 1g). Consistent with a previous study,[25] we also observed this MG–AIS interaction in the macaque neocortex (Supplementary information, Fig. S1), indicating that this type of interaction is conserved in primates. To further characterize the physical interaction between AISs and MGs, we obtained consecutive electron micrographs and performed 3D reconstruction of one PN–AISa-MG pair (Fig. 1h). We observed that the apposing cytoplasmic membranes of the AIS and microglial process ran virtually parallel and were separated by a very narrow extracellular space (Fig. 1i). Notably, the AIS and the process of the AISa-MG were bound together by some possible discrete linking structures (Fig. 1i), indicating that a tight and stable interaction may be formed between them.

Some AISa-MGs that interacted with the start of the neuronal AISs had their somata simultaneously in contact with the neuronal cell bodies (Fig. 1j, k), and these MGs were previously named satellite MGs.[25] We further divided the MGs into four groups based on whether the MGs and neurons had soma–soma and/or AIS–microglial process contacts: Ctrl, Soma-only, Soma&AIS, and AIS-only. Therefore, the aforementioned AISa-MGs included both the Soma&AIS and AIS-only groups of MGs (Fig. 1j, k). We found that there were ~45.15% Ctrl, ~28.90% Soma-only, ~15.61% Soma&AIS, and ~10.34% AIS-only MGs present in the neocortex (Fig. 1k). Intriguingly, we noticed that the somata of the majority of Soma-only MGs (~68.61%) contacted the apical dendrite side of the neuronal cell bodies, whereas somata of the Soma&AIS MGs exclusively contacted the axon side of the neuronal cell bodies (Fig. 1l). We next assessed the morphologies of these MG groups (Fig. 1m–o). Although the overall morphologies of these MG groups were ramified (Fig. 1j), the Soma-only, Soma&AIS, and AIS-only groups of MGs all had fewer intersections (Fig. 1m) and branches (Fig. 1n) compared with the Ctrl group. At the same time, the Soma-only MGs had the longest branch length, whereas the Soma&AIS MGs had the shortest branch length (Fig. 1o). Together, these results suggest that the Soma-only, Soma&AIS, and AIS-only MGs have some similar and distinct morphological features, presumably related to their interactions with different neuronal compartments.

To determine whether these groups represent molecularly distinct subpopulations of MGs, we performed transcriptomics by Patch-seq using *Cx3cr1-Cre^{ERT};YFP* mice (Fig. 2a). These mice had received in-utero intraventricular injection of rAAV-hSyn-AIS-mCherry-WPRE-pA virus at embryonic day 15–16 for visualization of physical contacts between MGs and the AISs of PNs after birth (Fig. 2a). Homeostatic MG markers, such as Tmem119, Serinc3, Sparc, Olfml3, P2ry12, Siglech, Selplg, C1qa, and Hexb, were all expressed in the four different MG groups (Fig. 2b). However, many homeostatic genes showed significantly reduced expression in the Soma-only MGs compared with the other groups (Fig. 2b), indicating that the Soma-only MGs tend to adopt reactive microglial features, as shown in some pathological conditions in previous studies.[24,33,34] Notably, we observed that the Soma-only, Soma&AIS, and AIS-only MGs had different sets of up- and downregulated genes (Fig. 2c; Supplementary information, Table S1), suggesting that they differ from each other in RNA expression profiles. However, at the same time, the Soma-only, Soma&AIS, and AIS-only groups shared some similar up- and downregulated genes at various levels (Fig. 2c, d). For example, the AIS-only and Soma&AIS MGs shared 17 upregulated genes, the Soma&AIS and Soma-only groups shared 12 upregulated genes, and the AIS-only and Soma-only MGs shared 7 upregulated genes (Fig. 2d). These upregulated genes shared between different groups of MGs may be related to their shared physical contacts with neurons. Indeed, upregulated genes shared by the AIS-only and Soma&AIS MGs showed significant associations with cell–cell adhesion and signaling (Fig. 2e), indicating that these MGs may have strong physical and functional cell–cell interactions, presumably with neurons through their shared contact with AISs.

We confirmed some of the shared upregulated genes in the AISa-MGs (including both the Soma&AIS and AIS-only groups) at the protein level by immunostaining (Fig. 2f; Supplementary information, Fig. S2). We found that the cell–cell adhesion protein integrin β1 (ITGB1), derived from the gene *Itgb1* (Fig. 2c, d), was more highly expressed on processes of AISa-MGs than on those of AISn-MGs (AIS-non-associated MGs, including both the Ctrl and Soma-only groups) (Fig. 2f, g). This result indicates that ITGB1 may play a role in mediating the physical interaction between microglial processes and neuronal AISs. Moreover, cytoplasmic expression of the intracellular signaling protein TMED2, derived from the gene *Tmed2* (Fig. 2c, d), was significantly increased in AISa-MGs instead of AISn-MGs (Supplementary information, Fig. S2a, b). Taken together, these data indicate that direct interactions with different neuronal compartments may have different effects on microglial transcriptomic profiles and that interaction with AISs can give AISa-MGs some specific transcriptomic fingerprints. Our data also suggest that some critical genes, such as *Itgb1* and *Tmed2*, may be involved in mediating the physical and functional interactions between MGs and neuronal AISs.

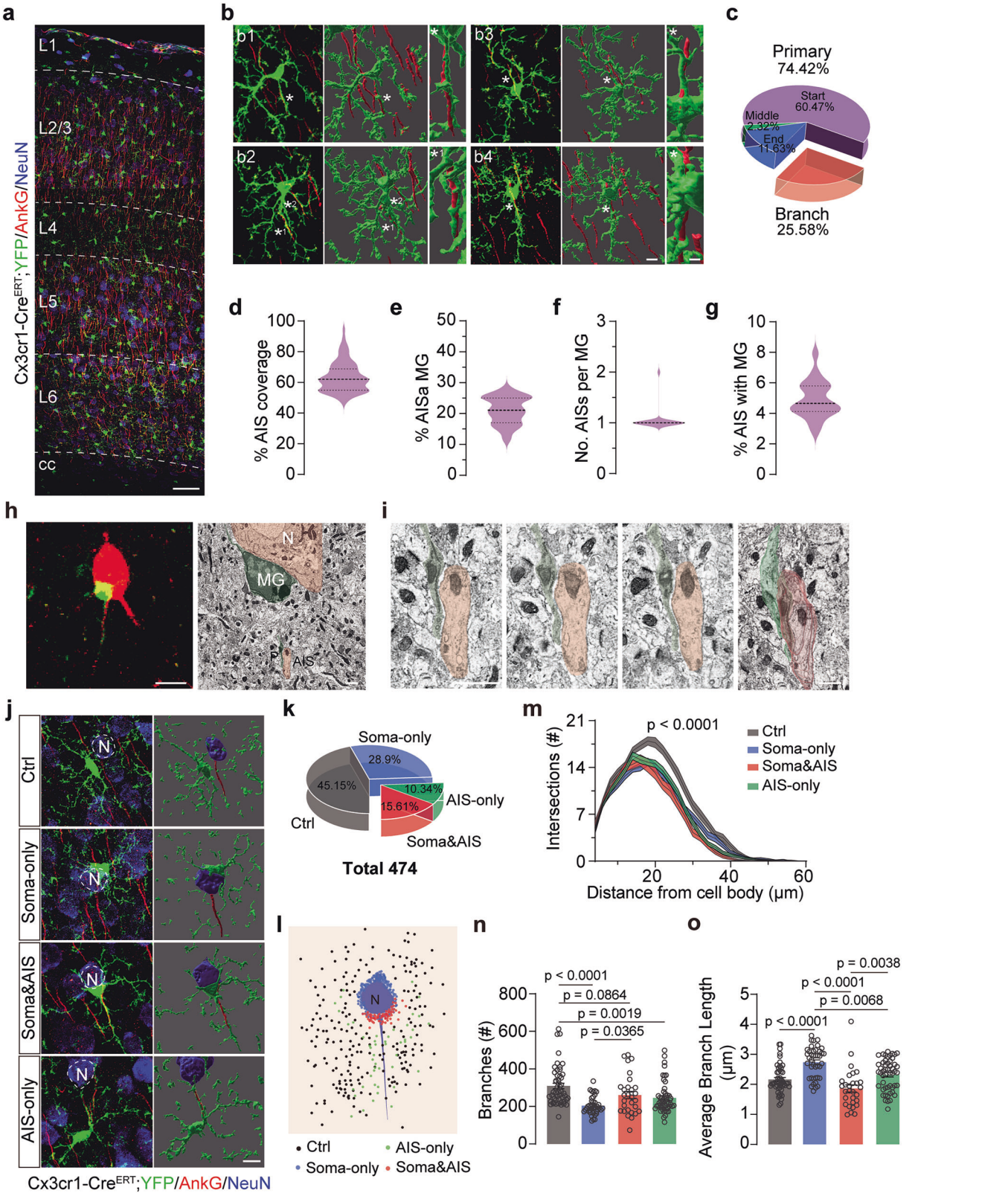

Brief depolarization of AISa-MGs specifically promotes AP firing of their associated PNs

To investigate whether direct interactions with MGs influence PN activity, we performed dual whole-cell recording of PNs and MGs simultaneously in layer 2/3 of V1 of ex vivo brain slices from 1–2-month-old *Cx3cr1-Cre*^{ERT}*;YFP* mice that had received in utero intraventricular injection of rAAV-hSyn-AIS-mCherry-WPRE-pA virus at embryonic day 15–16 (Fig. 3). The recordings were performed within 3 h after slice preparation, as in previous studies.[35,36] The overall morphologies of MGs and the physical

Fig. 1 Morphological characterization of MGs that interact with neuronal AISs in the neocortex. a Representative confocal image of MGs, neurons, and AISs in V1. Scale bar, 50 μm. **b** High-resolution images and 3D reconstructions of MGs interacting with AISs. Physical interactions between MGs and AISs are indicated by colored asterisks. Scale bars, 5 μm and 2 μm. **c** Percentages of AISa-MGs interacting with neurons at different positions (86 MGs from 21 views in V1 from 7 mice). **d** Percentage of AIS length covered by the microglial process and soma (69.39% ± 1.06%, 86 AISs from 7 mice). **e** Percentage of MGs interacting with AISs (21.03% ± 0.98%, 21 views from 7 mice). **f** Number of AISs interacting with 1 MG (1.05 ± 0.02, $n = 82$ cells from 7 mice). **g** Percentage of AISs associated with MGs (4.88% ± 0.27%, $n = 21$ views from 7 mice). **h** Confocal image and corresponding electron micrograph of one neuron (red) and its paired AISa-MG (green). N, neuron; P, microglial process. Scale bars, 10 μm and 1 μm. **i** Consecutive electron micrographs (left, 3 images) and 3D reconstruction (right) showing the tight physical contact between the AIS (red) and the microglial process (green) of the neuron/AISa-MG pair in **h**. Note the narrow extracellular space and discrete linking structures (indicated by cyan lines) formed between the AIS and the microglial process. Scale bars, 1 μm. **j** Representative confocal images and morphological reconstructions of different groups of MGs. Scale bar, 10 μm. **k** Percentages of different groups of MGs ($n = 7$ mice). **l** Diagram showing the soma center of different groups of MGs relative to the neuronal cell body and AIS. **m** Sholl analysis of the intersection number at different distances from cell bodies of different groups of MGs (Ctrl: $n = 49$ cells, Soma-only: $n = 41$ cells, Soma&AIS: $n = 29$ cells, AIS-only: $n = 51$ cells; two-sided two-way repeated-measures ANOVA). **n** Branch numbers of different groups of MGs (Ctrl: 309 ± 14.72, Soma-only: 204 ± 7.41, Soma&AIS: 261.10 ± 19.48, AIS-only: 245.80 ± 11.57; two-sided one-way ANOVA). **o** Average branch lengths of different groups of MGs (Ctrl: 2.16 ± 0.07, Soma-only: 2.74 ± 0.08, Soma&AIS: 1.86 ± 0.12, AIS-only: 2.32 ± 0.07; two-sided one-way ANOVA). Error bars indicate SEM.

interactions between PNs and MGs were largely well maintained, and no obvious cell apoptosis was observed within this time window, although sparse apoptosis signals were observed in MGs 5 h after slice preparation (Supplementary information, Fig. S3a–e). We found no chemical or electrical synaptic connections between PNs and MGs that had AIS–microglial process and/or soma–soma interactions (Supplementary information, Fig. S4a–d), suggesting that MGs could not directly influence neuronal activity through formation of chemical and electrical connections with PNs. Notably, the physical contacts between MGs and PNs were well preserved throughout the ~10-min recording time (Fig. 3a).

MGs are non-excitable cells whose functions are closely related to their MP fluctuations.[35,37,38] One previous whole-cell recording study reported 5–15-mV spontaneous transient depolarization of MGs in ex vivo brain slices.[39] To test whether brief depolarization of AISa-MGs influences PN activity, we modified their MPs by injecting a brief depolarizing current (500 ms, 10 pA) that induced an approximately 19.15-mV depolarization in the AISa-MGs (Fig. 3b, f). Concurrently, we injected 500-ms current steps from 0 pA to 150 pA with a 10-pA interval into PNs to induce AP firing (Fig. 3b). We found that a brief 10-pA current injection into an AISa-MG significantly increased the AP firing frequency of its associated PN (Fig. 3b, c). We then assessed the AP rheobase value and voltage threshold. In conjunction with the increased AP firing rate, the rheobase value was markedly lowered by injection of a 10-pA depolarizing current into the AISa-MG (Fig. 3d), whereas the AP voltage threshold remained the same (Fig. 3e). We also calculated the effect size of the increase in AP firing rate induced by the 10-pA current injection, which was 0.68 (Fig. 3f). As a control, a brief current injection into the MG did not cause obvious cell damage or induce cell apoptosis (Supplementary information, Fig. S3f). Likewise, repeated injections of current steps into PNs did not cause obvious cell damage (Supplementary information, Fig. S3f) or alter their AP firing frequency (Supplementary information, Fig. S3g, h). As a comparison, we injected a hyperpolarizing current into the AISa-MG and found that it did not influence AP firing of the associated PN (Supplementary information, Fig. S4e–h). We also recorded spontaneous excitatory postsynaptic currents (sEPSCs) and spontaneous inhibitory postsynaptic currents (sIPSCs) from PNs, with and without injection of a depolarizing current into the AISa-MGs. We found no difference in the amplitude or frequency of sEPSCs and sIPSCs (Fig. 3g–k), indicating that promotion of AP firing of PNs by AISa-MG depolarization did not occur through alteration of excitatory and inhibitory synaptic transmissions.

For comparison, we also recorded PN/MG pairs that did not have physical interactions (Supplementary information, Fig. S5a–e). In these pairs, injection of a brief depolarizing current into the AISn-MG did not change the frequency (Supplementary information, Fig. S5c) or electrophysiological properties of AP firing in the PN (Supplementary information, Fig. S5d, e). We also recorded several pairs of PNs and MGs that had physical contact between their somata (Soma-only pairs), which was confirmed by 3D reconstruction (Supplementary information, Fig. S5f–h). On average, ~28.09% of the area of the neuronal cell body contacted the MG somata (Supplementary information, Fig. S5f, g). As before, injection of a brief depolarizing current into these Soma-only MGs did not change the frequency or electrophysiological properties of AP firing in the PNs (Supplementary information, Fig. S5i–l). These results confirm that the promotion of AP firing of PNs by a brief depolarization of AISa-MG does not occur through soma–soma interactions or indirect pathways.

We next employed an optogenetic technique to manipulate microglial MPs by using *Cx3cr1-Cre^{ERT};Cheta-tdTomato* mice (Fig. 3l, m). Acute brain slices were prepared from these mice, and whole-cell recording of MGs was performed. We first confirmed that brief illumination (500 ms) with 470-nm light of moderate intensity induced MP depolarization by ~16.23 mV on average in MGs (Fig. 3n, o). Whole-cell recordings were then performed on PNs that physically interacted with microglial processes at the AISs. Current steps from 0 pA to 150 pA with a 10-pA interval were injected into PNs to trigger AP firing; concurrently, the 500-ms, 470-nm light was flashed to induce MG brief depolarization (Fig. 3p). Compared with the group without light stimulation (Off), the group that was illuminated with 470-nm light (On) showed a significant increase in AP firing frequency of PNs (Fig. 3q, r), and this was accompanied by a lower rheobase value (Fig. 3s) and an unchanged voltage threshold (Fig. 3t). The effect size of the increase in AP firing rate induced by this moderate illumination was 0.64 (Fig. 3u), similar to that induced by injection of a brief 500-ms, 10-pA depolarizing current into the AISa-MGs. The amplitude and frequency of sEPSCs and sIPSCs in PNs with or without illumination were comparable (Fig. 3v–z), confirming that the promotion of AP firing of PNs by a brief depolarization of AISa-MG does not occur through changes in excitatory and inhibitory synaptic transmissions. For comparison, we also recorded some PNs that had no direct contact (Supplementary information, Fig. S6a–i) or had soma–soma contact with MGs (Supplementary information, Fig. S6j–r). Global illumination with 470-nm light had no obvious effect on AP firing frequency, rheobase value, voltage threshold, or sEPSCs and sIPSCs of these PNs (Supplementary information, Fig. S6). Together, these data strongly suggest that MG depolarization selectively promotes AP firing of PNs through interactions with neuronal AISs but not with synapses, somata, or indirect pathways.

Release of intracellular K^+ through THIK-1 is essential for the promotion of neuronal activity by a brief depolarization of AISa-MG

Previous studies suggest that extracellular K^+ concentration is involved in the regulation of neuronal excitability.[31,32,40] Interestingly, one of the outward-rectifying two-pore-domain K^+ channels,

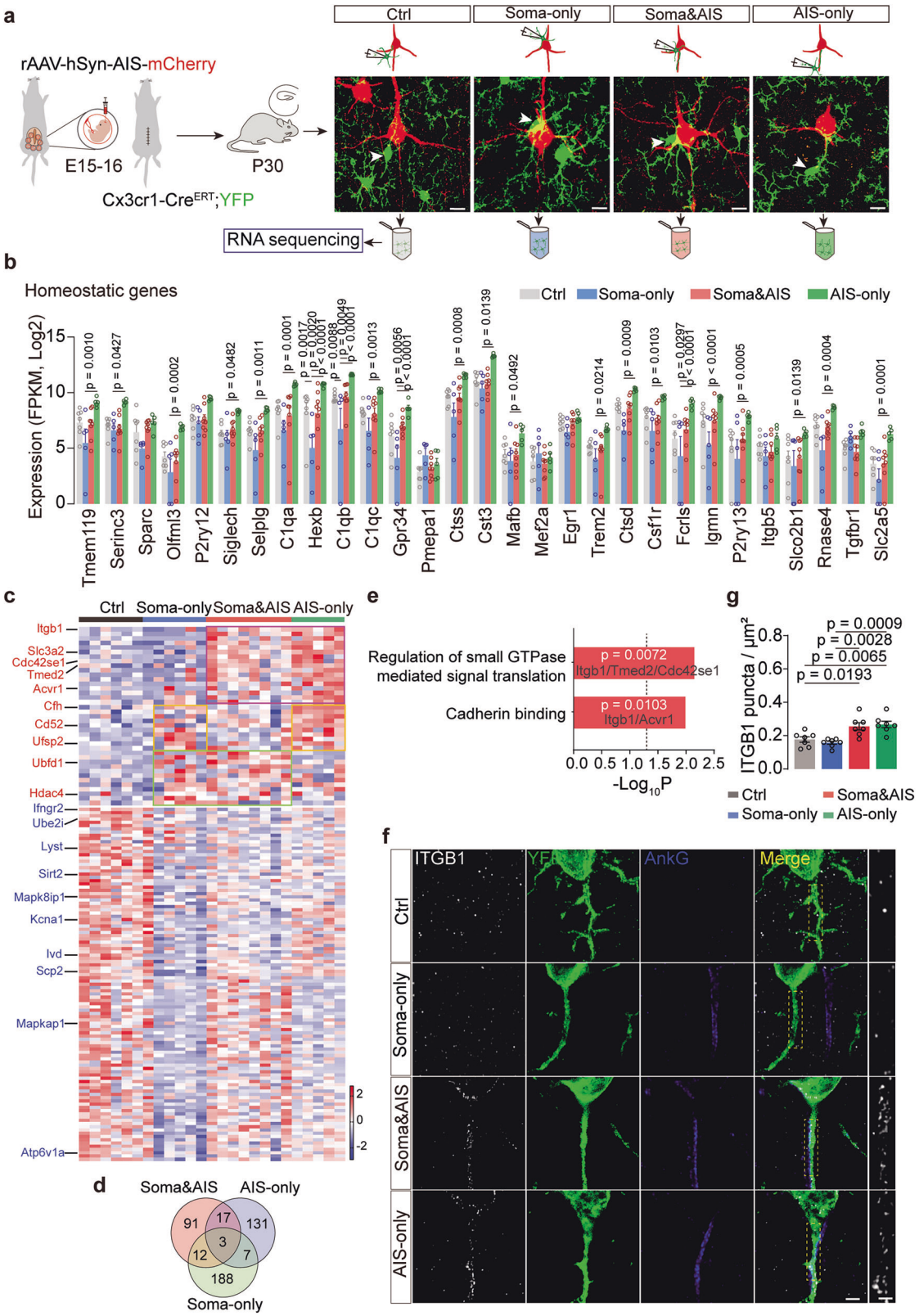

THIK-1, was recently found to be the main mediator of microglial outward K^+ current, which can counter-balance microglial depolarization and maintain the resting MP.[35] Re-analysis of previous RNA sequencing (RNA-seq) datasets revealed that THIK-1 mRNA is specifically expressed in human MGs[41,42] and mouse MGs and mature oligodendrocytes[1,43] (Supplementary information, Fig. S7a–c). We examined THIK-1 protein expression by immunostaining in layer 2/3 of V1 from 1–2-month-old mice and found that THIK-1 was specifically colocalized with MGs in *Cx3cr1-Cre^{ERT};YFP* mice but rarely colocalized with the astrocyte marker Aldh1l1 or

Fig. 2 AISa-MGs have a distinct transcriptomic profile. a Schematic of the experimental procedure used to collect cytoplasm and nucleus samples of different groups of MGs. Scale bar, 10 μm. **b** Expression of homeostatic MG signature genes in different groups of MGs ($n = 7$, 5, 8, and 5 batches from 3 mice for Ctrl, Soma-only, Soma&AIS, and AIS-only groups, respectively; two-sided Mann–Whitney test). **c** Heatmap showing upregulated and downregulated genes in different groups of MGs (Z-scored $\log_2$(FPKM + 1)). **d** Venn diagram showing overlaps of upregulated differentially expressed genes among different groups of MGs. **e** Selected gene ontology (GO) annotations for genes that were similarly upregulated in the AIS-only and Soma&AIS groups of MGs (dotted line, $P = 0.05$). **f** Confocal images showing ITGB1 protein expression on the processes of different groups of MGs. Dashed yellow box areas are further magnified on the right. Scale bars, 2 μm and 1 μm. **g** Quantification of ITGB1 protein expression in different groups of MGs (Ctrl: 0.18 ± 0.02, Soma-only: 0.16 ± 0.01, Soma&AIS: 0.26 ± 0.02, AIS-only: 0.27 ± 0.02; $n = 7$ mice; two-sided one-way ANOVA). Note that ITGB1 protein was highly expressed on the microglial processes that interacted with neuronal AISs. Error bars indicate SEM.

the neuron marker NeuN (Supplementary information, Fig. S7d, e). However, we did not observe obvious colocalization of THIK-1 with the oligodendrocyte lineage marker Oligo2, which labels oligodendrocyte precursor cells (OPCs) and immature and mature oligodendrocytes, in layer 2/3 of V1 from 1–2-month-old mice (Supplementary information, Fig. S7d). This was probably because mature oligodendrocytes are predominantly located in the white matter and deep layers of the mouse cortex, forming myelin sheaths around axons, and more than half of these mature oligodendrocytes are produced in the mouse brain after 4 months of age.[44,45]

We next hypothesized that AISa-MG depolarization may lead to K^+ release through THIK-1 specifically to the neuronal AIS and influence AP firing. To test this hypothesis, we used K^+-selective microelectrodes to study the concentration of K^+ released from microglial processes when MGs were depolarized by brief 500-ms, 470-nm illumination in ex vivo brain slices of *Cx3cr1-Cre^{ERT};YFP;Cheta-tdTomato* mice or current injections into MG in ex vivo brain slices of *Cx3cr1-Cre^{ERT};YFP* mice (Supplementary information, Fig. S8). After calibration in standard K^+ solutions of various concentrations (Supplementary information, Fig. S8b, c), the microelectrode was gently moved onto the microglial primary process (Supplementary information, Fig. S8d). We found that optogenetic illumination that induced ~16.23-mV depolarization in MGs (Fig. 3n, o) increased the K^+ concentration by ~1.86 mM (Supplementary information, Fig. S8e, f). Similarly, injection of a 10-pA current into MGs, which induced a ~19.15-mV depolarization (Fig. 3f), increased the K^+ concentration by ~1.83 mM (Supplementary information, Fig. S8g, h). Notably, the increases in K^+ concentration were almost completely abolished by 50 μM of the THIK-1 inhibitor TPA, 5 μM of the THIK-1 specific antagonist C101248, or THIK-1 conditional knockout (cKO) in MGs of *Cx3cr1-Cre^{ERT};YFP;Cheta-tdTomato;THIK-1$^{fl/fl}$* (Cheta;cKO) and *Cx3cr1-Cre^{ERT};YFP;THIK-1$^{fl/fl}$* (cKO) mice (Supplementary information, Fig. S8e–h). Together, these results suggest that MG depolarization triggered by different stimuli can similarly induce intracellular K^+ release through the THIK-1 channel.

To further test whether the intracellular K^+ release induced by MG depolarization influences AP firing of PNs, we performed dual whole-cell recording of a single PN using normal internal solution and its AISa-MG using a K^+-free internal solution ($-K^+$) to diminish intracellular K^+ release (Fig. 4a–e). As expected, depletion of intracellular K^+ from MGs eliminated the facilitation of AP firing in PNs induced by AISa-MG depolarization (Fig. 4c). In addition, depletion of intracellular K^+ significantly increased the AP rheobase value (Fig. 4d) but did not influence the AP voltage threshold (Fig. 4e). These results suggest that promotion of neuronal AP firing rate by brief depolarization of the AISa-MG is dependent on microglial intracellular K^+ release.

To further investigate whether release of K^+ directly to the AISs influences the AP firing of PNs, we recorded PNs in layer 2/3 in V1 and puffed 5 mM K^+ (2 mM more than the baseline concentration of 3 mM) directly onto the AISs (Fig. 4f). Puffing of K^+ onto the AISs induced a prominent sub-threshold depolarization of PNs (Fig. 4g, i). As predicted, the AP firing frequency was markedly increased when K^+ was puffed directly onto the AISs (Fig. 4h, j), indicating that K^+ release directly onto the AISs indeed promotes neuronal AP firing by inducing a sub-threshold depolarization of PNs.

To confirm whether MG depolarization indeed induces a sub-threshold depolarization of PNs specifically at the AISs through THIK-1, we used the MP indicator ASAP3,[46,47] by injecting AAV-CaMKIIα-ASAP3 into V1 of *TMEM119-Cre^{ERT};Cheta-tdTomato* mice. These mice received intraperitoneal injections of tamoxifen for 5 consecutive days to induce Cheta-tdTomato expression specifically in MGs before two-photon imaging (Supplementary information, Fig. S9a). We identified some pairs of MGs and PNs with soma–soma interactions in vivo, which were confirmed by in vitro immunostaining after two-photon imaging (Supplementary information, Fig. S9b). We applied single-cell optogenetic stimulation of 200-ms, 940-nm light onto the Soma-only MGs; however, we observed no obvious MP changes in the associated PNs (Supplementary information, Fig. S9c, d). We also identified some pairs of MGs and PNs with AIS–microglial process interactions, which were also confirmed by immunostaining after two-photon imaging (Supplementary information, Fig. S9e, h). This time, single-cell optogenetic stimulation of AISa-MGs induced robust MP depolarization in the associated PNs. The depolarization was restricted to the small area of the soma–AIS interface and was blocked by the THIK-1 specific antagonist C101248[41] (Supplementary information, Fig. S9e–m). By contrast, optogenetic stimulation of nearby AISn-MGs did not induce obvious MP depolarization in PNs (Supplementary information, Fig. S9e–m). These results indicate that brief depolarization of AISa-MG can indeed induce MP depolarization of associated PNs specifically at the soma–AIS interface through THIK-1 channels.

To investigate whether THIK-1 activity is indeed needed for promotion of AP firing in PNs by AISa-MG depolarization, we first examined the RNA expression and spatial distribution of THIK-1. THIK-1 mRNA copy number was significantly higher in the AISa-MGs than in AISn-MGs (Fig. 4k), and THIK-1 channels were more abundant on microglial processes that interacted with neuronal AISs (Fig. 4l, m). We next modulated THIK-1 opening in dual whole-cell recording experiments. We applied 5 μM of the THIK-1 specific antagonist C101248 for a short duration of 10 min, which had no obvious effect on the MG–AIS interaction (Fig. 4n, o). Dual whole-cell recordings were performed on pairs of PNs and AISa-MGs, with or without addition of C101248 in the MG internal solution to block K^+ release through THIK-1 (Fig. 4r). As previously reported,[35] microglial MP was dramatically depolarized by THIK-1 blockade (Fig. 4s). Similarly, blockade of microglial THIK-1 eliminated facilitation of AP firing in PNs by the brief depolarization of AISa-MG (Fig. 4t); it also significantly increased the rheobase value (Fig. 4u) but did not change the AP voltage threshold (Fig. 4v), indicating that THIK-1 activity is indeed needed for promotion of AP firing of associated PNs by the brief depolarization of AISa-MG, presumably through release of intracellular K^+.

THIK-1 KO has been reported to dramatically alter microglial morphology and ramification.[35] This was confirmed in our experiments using *Cx3cr1-Cre^{ERT};YFP;THIK-1$^{fl/fl}$* (cKO) mice after 5 consecutive days of tamoxifen administration, which induced a dramatic reduction in THIK-1 expression in MGs (Supplementary

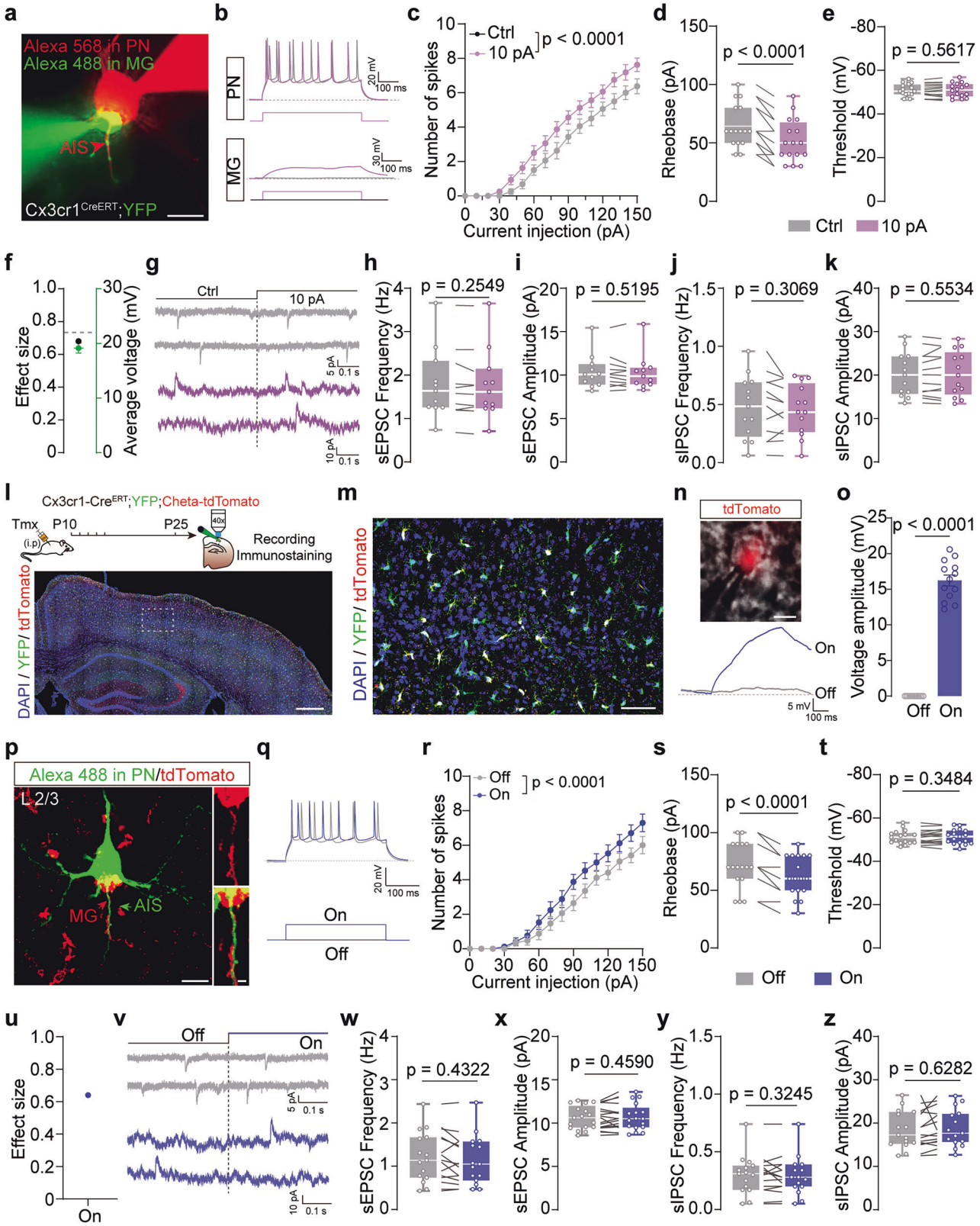

information, Fig. S10a, b) and morphological simplification (Supplementary information, Fig. S10c–g). Unlike THIK-1 straight KO mice,[48] THIK-1 cKO mice did not show obvious changes in excitatory and inhibitory synapse numbers and synaptic transmissions (Supplementary information, Fig. S10i–s), probably because of the short-time THIK-1 ablation. Surprisingly, THIK-1 cKO did not affect the physical contacts between MGs and neuronal AISs (Fig. 4p, q). We then performed dual recordings of PNs and associated AISa-MGs in brain slices of THIK-1 cKO mice (Fig. 4w). The microglial MP was markedly depolarized after THIK-1 cKO

Fig. 3 Brief depolarization of AISa-MGs promotes AP firing of their associated PNs. a Representative image showing a dual whole-cell recording of one MG-PN pair that physically interacted at the AIS. PNs were filled with Alexa 568, and MGs were filled with Alexa 488. MGs were injected with a 10-pA current, and PNs were concurrently injected with current steps from 0 pA to 150 pA with a 10-pA interval to induce AP firing. Scale bar, 10 μm. **b** Sample traces of the recorded AISa-MG and PN pair in **a**. **c** AP numbers of PNs ($n = 16$ pairs from 5 mice; two-sided two-way repeated-measures ANOVA). **d** Rheobase values of AP firing in PNs (10 pA: 51.88 pA ± 4.58 pA vs Ctrl: 64.38 pA ± 4.56 pA; two-sided paired *t*-test). **e** Voltage thresholds of AP firing in PNs (10 pA: –50.96 mV ± 0.80 mV vs Ctrl: –50.87 mV ± 0.72 mV; two-sided paired *t*-test). **f** Effect size of the increase in AP firing rate in PNs and voltage change in MGs induced by injection of a 10-pA depolarizing current into the AISa-MG. **g** Example traces of sEPSCs and sIPSCs recorded from PNs with or without 10-pA current injection into the AISa-MG. **h**, **i** Frequency (Depolarizing: 1.78 Hz ± 0.24 Hz vs Ctrl: 1.80 Hz ± 0.25 Hz; $n = 11$ cells from 4 mice; two-sided paired *t*-test) and amplitude (Depolarizing: 10.30 pA ± 0.63 pA vs Ctrl: 10.40 pA ± 0.61 pA; two-sided Wilcoxon matched-pairs signed-rank test) of sEPSCs. **j**, **k** Frequency (Depolarizing: 0.45 Hz ± 0.06 Hz vs Ctrl: 0.48 Hz ± 0.07 Hz; $n = 13$ cells from 4 mice; two-sided paired *t*-test) and amplitude (Depolarizing: 20.34 pA ± 1.44 pA vs Ctrl: 20.21 pA ± 1.39 pA; two-sided paired *t*-test) of sIPSCs. **l**, **m** Schematic of the experimental procedure and confocal images of MGs expressing Cheta-tdTomato, colocalized with YFP. Scale bars, 400 μm and 50 μm. **n** Representative image of a recorded MG (upper). MP depolarization in response to illumination with 470-nm moderate-intensity light (lower). Scale bar, 5 μm. **o** Voltage changes in MGs in response to moderate-light illumination (On: 16.23 mV ± 0.77 mV; $n = 13$ cells from 5 mice; two-sided Mann–Whitney test). **p** Representative images of one recorded PN that was associated with an MG at the AIS and received moderate-light illumination. Scale bars, 10 μm and 2 μm. **q** Sample traces of the recorded PN in **p**. **r** AP numbers of PNs ($n = 17$ pairs from 5 mice; two-sided two-way repeated-measures ANOVA with multiple comparisons). **s** Rheobase values of AP firing in PNs (On: 62.35 pA ± 4.25 pA vs Off: 71.76 pA ± 4.79 pA; $n = 17$ pairs from 5 mice; two-sided paired *t*-test). **t** Voltage thresholds of AP firing in PNs (On: –51.32 mV ± 0.79 mV vs Off: –51.12 mV ± 0.76 mV, $n = 17$ pairs from 5 mice; two-sided paired *t*-test). **u** Effect size of the increase in AP firing rate in PNs induced by moderate-light illumination. **v** Example traces of sEPSCs and sIPSCs recorded from PNs associated with MGs at the AISs, with or without illumination. **w**, **x** Frequency (On: 1.17 Hz ± 0.13 Hz vs Off: 1.21 Hz ± 0.13 Hz; $n = 17$ cells from 4 mice; two-sided paired *t*-test) and amplitude (On: 10.70 pA ± 0.37 pA vs Off: 10.61 pA ± 0.33 pA; $n = 17$ cells from 4 mice; two-sided paired *t*-test) of sEPSCs. **y**, **z** Frequency (On: 0.30 Hz ± 0.04 Hz vs Off: 0.31 Hz ± 0.04 Hz; $n = 17$ cells from 4 mice; two-sided paired *t*-test) and amplitude (On: 19.51 pA ± 1.18 pA vs Off: 19.17 pA ± 1.09 pA; $n = 17$ cells from 4 mice; two-sided paired *t*-test) of sIPSCs. Whiskers of box plots extend to the 2.5th and 97.5th percentiles of the data. Error bars indicate SEM.

(Fig. 4x), and the input resistance was significantly increased (Supplementary information, Fig. S10h) owing to a lack of tonic THIK-1 conductance. A brief depolarization of AISa-MGs no longer promoted AP firing of associated PNs in THIK-1 cKO group compared with the wild-type (WT) group (Fig. 4y). THIK-1 cKO significantly increased the rheobase value (Fig. 4z) but did not change the AP threshold in the associated PNs (Fig. 4aa). These results further confirm that THIK-1 activity is needed for promotion of AP firing of associated PNs by brief depolarization of AISa-MGs.

In addition to THIK-1, MGs also express other types of outward K^+ channels, such as Kv1.3, which is only activated under inflammatory conditions.[38,49,50] We therefore investigated whether blockade of Kv1.3 in AISa-MGs by its specific antagonist PAP-1 would influence the AP firing of PNs. Our data showed that inhibition of microglial Kv1.3 did not affect the promotion of AP firing of PNs by brief depolarization of AISa-MG (Supplementary information, Fig. S11). Together, our results demonstrate that the facilitation of AP firing of associated PNs induced by AISa-MG depolarization probably occurs through THIK-1-dependent K^+ release to modulate local MP at the AISs.

Visual stimulation with drifting gratings induces transient depolarizing events in MGs

Thus far, our results suggested that MG brief depolarization can promote AP firing of PNs specifically through interactions with neuronal AISs. However, whether transient depolarization of MGs occurs in vivo under physiological conditions was unknown, as were its underlying mechanisms. To address these questions, we used the MP indicator ASAP3 to monitor MP fluctuations in MGs. We first verified that ASAP3 fluorescence intensity responded to and was negatively correlated with MP depolarization induced by application of the THIK-1 antagonist TPA to primary cultured MGs (Supplementary information, Fig. S12a–c), consistent with previous studies.[46,47] We then generated an ASAP3 reporter mouse line and crossed it with a TMEM119-Cre line to obtain *TMEM119-Cre;ASAP3* mice and confirmed specific expression of ASAP3 in MGs (Fig. 5a, b). We performed whole-cell recordings combined with time-lapse imaging in ex vivo brain slices from *TMEM119-Cre;ASAP3* mice. By holding the MP at various levels by perfusing artificial cerebrospinal fluid (ACSF) with different concentrations of KCl, we determined the negative correlation between ASAP3 fluorescence intensity and microglial MP within the –40–0 mV range (Fig. 5c–f). Next, we performed two-photon imaging combined with visual stimulation using drifting gratings on head-fixed awake *TMEM119-Cre;ASAP3* mice (Fig. 5g). The visual stimulation induced transient depolarizing events in MGs (Fig. 5h, i). Notably, these transient depolarizing events were more robust on processes than on somata of MGs (Fig. 5h, i). The amplitude of these transient depolarizing events was ~17.33 mV on average (10–23 mV) (Fig. 5i, right), slightly larger than that of spontaneous transient depolarization recorded from MGs in ex vivo brain slices.[39] Importantly, after THIK-1 cKO in MGs of *TMEM119-Cre;ASAP3;THIK-1$^{fl/fl}$* (cKO;ASAP3) mice, transient depolarizing events could still be induced by visual stimulation, but MP failed to recover normally to a resting level after stimulation (Fig. 5j, k). These results suggest that visual stimulation can induce transient depolarization of MGs that occurs mainly on their processes under physiological conditions and that K^+ release through THIK-1 plays a critical role in restoring resting MP after this transient depolarization.

We next studied what induces the depolarizing events in MGs in response to visual stimulation. Previous work has shown that MGs express several types of G protein-coupled receptors (GPCRs), such as P2Y12Rs, muscarinic receptors, and adrenergic receptors, and these GPCRs regulate microglial functions differently under various conditions.[24,35,36,51–56] We first used ticagrelor to specifically block P2Y12Rs.[57] However, we found that P2Y12R blockade did not affect the transient depolarizing events of MGs in response to visual stimulation (Supplementary information, Fig. S12d, e). Similarly, inhibition of adrenergic receptors by their antagonist propranolol[51] also had no obvious effect on these transient depolarizing events (Supplementary information, Fig. S12f, g). We then applied scopolamine to specifically block muscarinic receptors[58] and found that it greatly reduced the transient depolarization events of MGs (Fig. 5l, m; Supplementary information, Video S1). Together, our results suggest that muscarinic receptors, but not P2Y12Rs or adrenergic receptors, mediate microglial depolarizing activity in response to visual stimulation under physiological conditions.

We next asked which cation channel directly mediated microglial transient depolarization under physiological conditions. We found that mRNA copy number of *Nalcn*, which encodes the TTX-insensitive Na^+ channel NALCN, was significantly increased in AISa-MGs (Fig. 5n). We confirmed that NALCN was indeed more

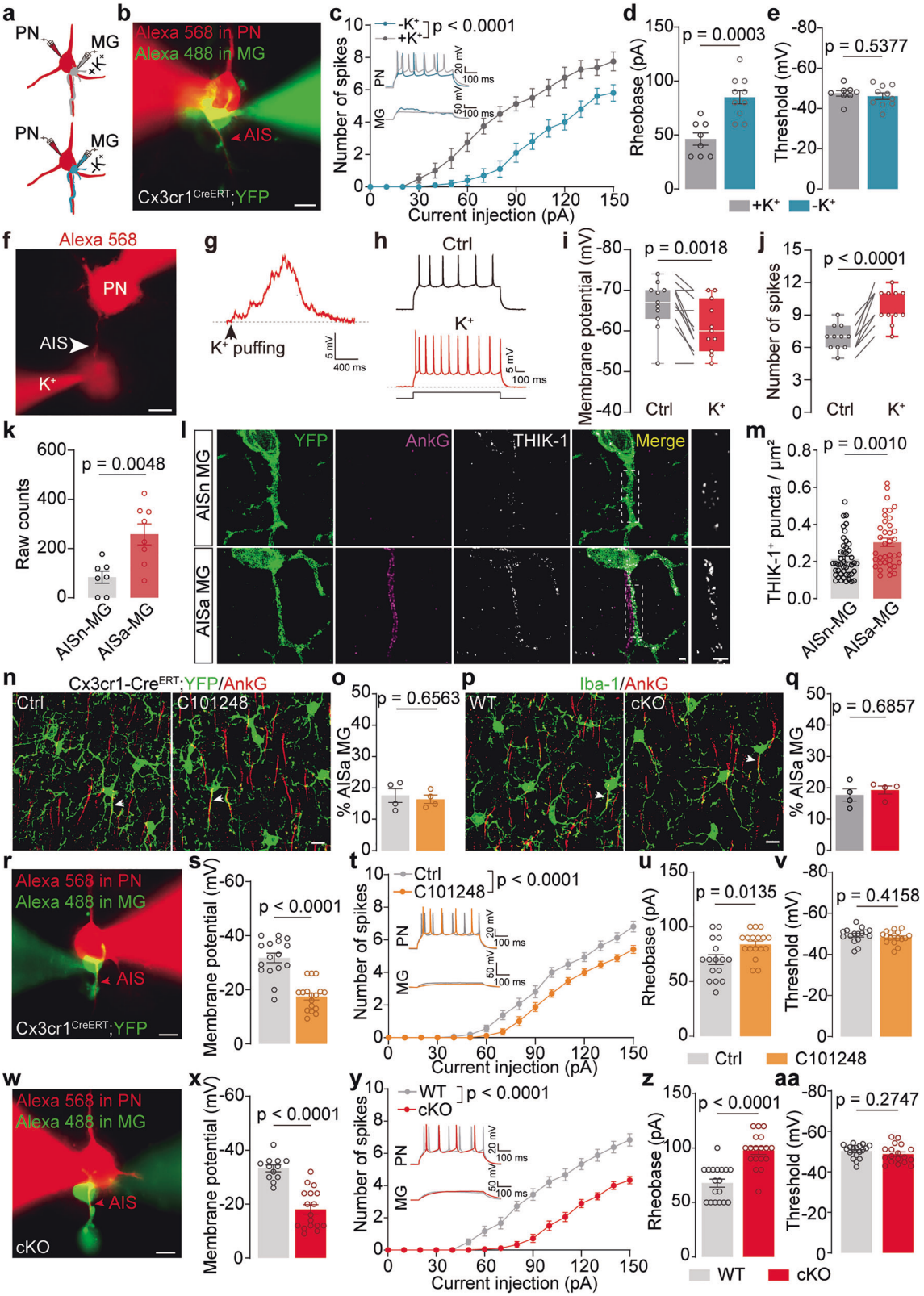

highly expressed on the microglial processes that interacted with neuronal AISs (Fig. 5o, p). Previous studies have shown that NALCN can be activated by muscarinic receptors,[59,60] and it was therefore possible that NALCN mediates microglial transient depolarization induced by visual stimulation. To test this possibility, we used CP96345 to specifically block NALCN[61] and found that CP96345 greatly reduced the transient depolarization events of MGs (Fig. 5q, r), suggesting that microglial transient depolarization induced by visual stimulation may be directly mediated by the Na^+ channel NALCN.

Fig. 4 Intracellular K^+ release from AISa-MGs through THIK-1 promotes AP firing of the associated PNs. a Schematic of the experimental procedure. **b** Representative image of a dual whole-cell recording of one MG-PN pair that interacted physically at the AIS. Scale bar, 10 μm. **c** AP numbers of PNs ($+K^+$: $n = 8$ pairs from 3 mice vs $-K^+$: $n = 10$ pairs from 4 mice; two-sided two-way repeated-measures ANOVA). Insets are sample traces of paired AISa-MGs and PNs with the AISa-MG recorded using $+K^+$ or $-K^+$ internal solution. **d** Rheobase values of AP firing in PNs ($+K^+$: 46.25 pA ± 5.65 pA vs $-K^+$: 85.00 pA ± 6.01 pA; two-sided unpaired *t*-test). **e** Voltage thresholds of AP firing in PNs ($+K^+$: −47.54 mV ± 1.40 mV vs $-K^+$: −46.13 pA ± 1.65 pA; two-sided unpaired *t*-test). **f** Representative image of a whole-cell recording of one PN with 5 mM K^+ puffed onto its AIS. Scale bar, 10 μm. **g** Sample trace showing the MP change of the recorded PN. **h** Sample traces of AP firing of the recorded PN in **g**. **i** Peak MP change of PNs (K^+: −61.00 mV ± 1.94 mV vs Ctrl: −66.31 mV ± 1.85 mV, $n = 11$ cells from 4 mice; two-sided paired *t*-test). **j** AP numbers of PNs (K^+: 9.73 ± 0.47 vs Ctrl: 6.91 ± 0.34, $n = 11$ cells from 4 mice; two-sided paired *t*-test). **k** mRNA copy numbers of the THIK-1 coding gene *Kcnk13* in AISa-MGs vs AISn-MGs (AISa-MG: 258.10 ± 42.86, $n = 8$ mice vs AISn-MG: 83.57 ± 24.53, $n = 7$ mice; two-sided unpaired *t*-test). **l** Confocal images showing THIK-1 expression on the microglial primary process that interacted with the neuronal AIS. Scale bar, 1 μm. **m** Quantification of THIK-1 protein expression on the processes of AISa-MGs vs AISn-MGs (AISa-MG: 0.30 ± 0.02, $n = 37$ cells vs AISn-MG: 0.21 ± 0.02, $n = 45$ cells from 5 mice; two-sided Mann–Whitney test). **n** Representative confocal images showing the physical interactions between AISs and MGs, with or without C101248 application; Scale bar, 10 μm. **o** Percentages of MGs interacting with neuronal AISs (C101248: 16.40% ± 1.31%, $n = 4$ mice vs Ctrl: 17.60% ± 2.20%, $n = 4$ mice; two-sided unpaired *t*-test). **p** Representative confocal images showing physical interactions between AISs and MGs in WT vs THIK-1 cKO mice. Scale bar, 10 μm. **q** Percentages of MGs interacting with neuronal AISs (cKO: 18.30% ± 1.29%, $n = 4$ mice vs WT: 17.70% ± 1.96%, $n = 4$ mice; two-sided Mann–Whitney test). **r** Representative image of a dual whole-cell recording of one MG-PN pair that interacted physically at the AIS. Scale bar, 10 μm. **s** Quantification of microglial MPs (C101248: −17.48 mV ± 1.26 mV, $n = 17$ cells from 4 mice vs Ctrl: −31.78 mV ± 1.76 mV, $n = 16$ cells from 4 mice; two-sided unpaired *t*-test). **t** AP numbers of PNs (Ctrl, $n = 16$ pairs from 4 mice vs C101248, $n = 17$ pairs from 4 mice; two-sided two-way repeated-measures ANOVA). Insets are sample traces of dual recordings. **u** Rheobase values of AP firing in PNs (C101248: 84.12 pA ± 2.98 pA, $n = 17$ cells from 4 mice vs Ctrl: 70.00 pA ± 4.56 pA, $n = 16$ cells from 4 mice; two-sided unpaired *t*-test). **v** Voltage thresholds of AP firing in PNs (C101248: −48.38 mV ± 0.74 mV, $n = 17$ cells from 4 mice vs Ctrl: −49.33 mV ± 0.90 mV, $n = 16$ cells from 4 mice; two-sided unpaired *t*-test). **w** Representative images of a dual whole-cell recording of one MG-PN pair from a THIK-1 cKO mouse. Scale bar, 10 μm. **x** Quantification of microglial MP (cKO: −18.06 mV ± 1.77 mV, $n = 17$ cells from 4 mice vs WT: −33.25 mV ± 1.25 mV, $n = 12$ cells from 4 mice; two-sided unpaired *t*-test). **y** AP numbers of PNs ($n = 18$ pairs from 4 mice in both cKO and WT groups; two-sided two-way repeated-measures ANOVA). Insets are sample traces of dual recordings. **z** Rheobase values of AP firing in PNs (cKO: 97.78 pA ± 3.67 pA vs WT: 67.78 pA ± 3.67 pA, $n = 18$ cells from 4 mice; two-sided Mann–Whitney test). **aa** Voltage thresholds of AP firing in PNs (cKO: −48.81 mV ± 1.10 mV vs WT: −50.37 mV ± 0.78 mV, $n = 18$ cells from 4 mice; two-sided unpaired *t*-test). Error bars indicate SEM. Whiskers of box plots extend to the 2.5th and 97.5th percentiles of the data.

The functional interaction between AISa-MGs and PNs regulates the calcium responses of the associated PNs and thus affects visual discrimination behavior

We next examined whether the functional interaction between AISa-MGs and PNs is involved in higher-order brain functions. Calcium imaging combined with visual stimulation using drifting gratings was performed on head-fixed awake mice under a two-photon microscope. These mice were injected with rAAV2/9-CaMKIIα-GCaMp6f-pA virus into V1 layer 2/3 (Fig. 6a; Supplementary information, Fig. S13a). We identified neural ensembles that responded to drifting gratings with different orientations (Supplementary information, Fig. S13b–d) as described previously.[62,63] We first administered 5 μM of the THIK-1 antagonist C101248 into V1 layer 2/3 10 min before two-photon calcium imaging (Fig. 6a). Application of C101248 resulted in a significant decrease in the peak ΔF/F (Fig. 6b, d) and frequency (Fig. 6c, d) of calcium transients in PNs of the neural ensembles. Notably, we identified a greater decline in peak ΔF/F (Fig. 6b, right) and frequency (Fig. 6c, right) of calcium transients in a small portion of PNs that responded more robustly to visual stimulation (strongly responding PNs) upon C101248 application (Supplementary information, Video S2). Interestingly, THIK-1 cKO in MGs in brains of *Cx3cr1-Cre^{ERT};YFP;THIK-1$^{fl/fl}$* mice led to a selective disappearance of some strongly responding PNs, and application of C101248 into V1 layer 2/3 of these THIK-1 cKO mice no longer affected neuronal calcium responses to visual stimulation (Supplementary information, Fig. S14a–d). As a control, C101248 did not directly affect the calcium transients of cultured primary neurons in vitro (Supplementary information, Fig. S15). Previous RNA-seq datasets showed that THIK-1 mRNA is expressed in mature oligodendrocytes as well as MGs (Supplementary information, Fig. S7a–c); however, we observed only very weak colocalization of THIK-1 with the mature myelin marker MBP at the protein level in layer 2/3 of V1 of 1–2-month-old mice (Supplementary information, Fig. S14e–g), in striking contrast to the strong expression in MGs (Supplementary information, Fig. S7e). We then applied C101248 to V1 layer 2/3 of *NG2-Cre;THIK-1$^{fl/fl}$* mice, in which THIK-1 ablation is driven in the oligodendrocyte lineage, including OPCs and immature and mature oligodendrocytes.[64,65] THIK-1 cKO in the oligodendrocyte lineage significantly reduced colocalization of THIK-1 with MBP but did not affect overall MBP distribution in the cortex (Supplementary information, Fig. S14e–g). We also found that calcium transients of PNs responding to visual stimulation were still significantly inhibited by C101248 in *NG2-Cre;THIK-1$^{fl/fl}$* mice (Supplementary information, Fig. S14h–k), suggesting that the influence of C101248 on neuronal calcium responses does not occur through inhibition of THIK-1 channels in oligodendrocytes. In comparison, application of the P2Y12R specific antagonist ticagrelor had no obvious effect on the ΔF/F and frequency of calcium transients in PNs responding to visual stimulation (Supplementary information, Fig. S16a–c). Together, these results suggest that the THIK-1 specific antagonist C101248 reduces neuronal calcium responses through specific inhibition of THIK-1 channels in MGs rather than in oligodendrocytes and neurons.

We next used an optogenetic method to suppress the microglial depolarizing activity induced by visual stimulation by injecting rAAV2/9-CaMKIIα-GCaMp6f-pA virus into V1 layer 2/3 of *TMEM119-Cre^{ERT};Ai40D* mice (Supplementary information, Fig. S17). We confirmed that optogenetic illumination with 593-nm light hyperpolarized microglial MP in brain slices (Supplementary information, Fig. S17a–c). Similarly, 593-nm illumination significantly reduced the ΔF/F and frequency of calcium transients in PNs of the neural ensembles, and the ΔF/F and frequency of calcium transients were more dramatically reduced in a small portion of strongly responding PNs upon illumination (Supplementary information, Fig. S17d–f). We performed immunostaining on in vitro, horizontally cut brain slices from mice that had undergone in vivo calcium imaging in order to identify PNs that interacted with MGs at the AISs (AISa-PNs) and nearby PNs that did not interact with MGs at the AISs (AISn-PNs) (Supplementary information, Fig. S17g–k). Interestingly, the AISa-PNs showed more robust ΔF/F and frequency of calcium transients in response to visual stimulation compared with nearby AISn-PNs (Supplementary information, Fig. S17l–n). In addition, a specific reduction in the ΔF/F and frequency of calcium transients was observed in AISa-PNs compared with nearby AISn-PNs upon optogenetic

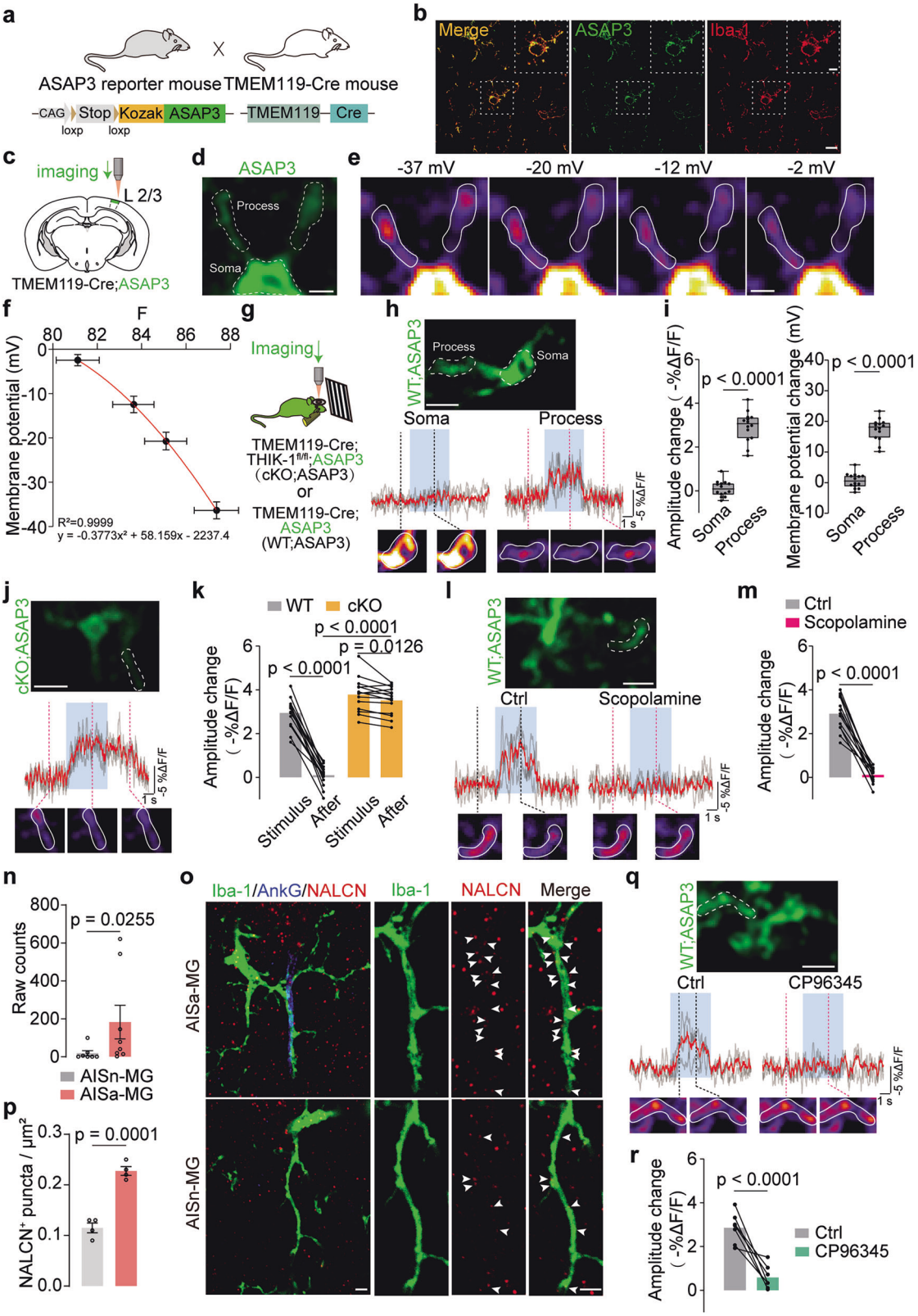

illumination with 593-nm light to suppress microglial depolarizing activity (Supplementary information, Fig. S17l–n, Video S3). This result suggested that microglial depolarizing activity specifically enhances the calcium transient responses of a small portion of PNs that interact with MGs at the AISs in neural ensembles.

To further confirm that AISa-PNs and AISn-PNs respond differently to visual stimulation, we performed two-photon calcium imaging of *Cx3cr1-Cre^{ERT};YFP* mice that were injected with rAAV-CaMKIIα-NES-jRGECO1α and rAAV-hSyn-AIS-m Cherry-WPRE-pA virus (Fig. 6e; Supplementary information, Fig. S18). We

Fig. 5 In vivo visual stimulation with drifting gratings induces transient depolarizing events selectively on microglial processes. **a** Schematic of the experimental procedure for generation of *TMEM-Cre;ASAP3* knock-in mice. **b** Immunostaining images confirming ASAP3 expression in MGs. Scale bars, 10 μm and 5 μm. **c** Schematic of the experimental procedure for ex vivo two-photon imaging of ASAP3 signals in MGs of acute brain slices. **d**, **e** Representative images of ASAP3 signals on the somata and processes of MGs in response to different voltages resulting from perfusion of ACSF with different KCl concentrations. Scale bar, 5 μm. **f** Negative correlation between ASAP3 fluorescence intensity and MP. **g** Schematic of the experimental procedure for in vivo two-photon ASAP3 imaging. **h** Example of ASAP3 fluorescence changes in the soma and process of an MG from a WT mouse induced by visual stimulation. Scale bar, 10 μm. **i** Left: amplitude changes of ASAP3 signals in the soma and process (Soma: 0.10 ± 0.10 vs Process: 2.93 ± 0.19, $n = 14$ cells from 5 mice; two-sided unpaired *t*-test) of MGs in WT mice. Right: MP changes in the soma and process (Soma: 0.64 mV ± 0.65 mV vs Process: 17.33 mV ± 0.96 mV, $n = 14$ cells from 5 mice; two-sided unpaired *t*-test) of MGs in WT mice. **j** Example of ASAP3 fluorescence changes in the process of an MG in a THIK-1 cKO mouse induced by visual stimulation. Scale bar, 10 μm. **k** Quantification of the amplitude change of ASAP3 signals in the processes of MGs in WT and THIK-1 cKO mice during and after visual stimulation (WT: Stimulus: 2.93 ± 0.19 vs After: 0.09 ± 0.13, $n = 14$ cells from 5 mice; two-sided paired *t*-test. cKO: Stimulus: 3.78 ± 0.21 vs After: 3.52 ± 0.17, $n = 14$ cells from 5 mice; two-sided paired *t*-test. After: WT vs cKO, two-sided unpaired *t*-test). Note that the dataset of WT stimulus group is shared with that of the Process group in the left panel in **i**. **l** Representative images of ASAP3 signals on the processes of MGs responding to visual stimulation, before and after injection of the muscarinic receptor specific blocker scopolamine. Scale bar, 10 μm. **m** Amplitude changes in ASAP3 signals before and after scopolamine application (Ctrl: 2.91 ± 0.22 vs Scopolamine: 0.11 ± 0.10; two-sided paired *t*-test; $n = 13$ cells from 5 mice). **n** mRNA copy number of the NALCN coding gene *Nalcn* in AISa-MGs vs AISn-MGs (AISa-MG: 182.60 ± 88.83, $n = 8$ mice vs AISn-MG: 18.14 ± 13.85, $n = 7$ mice; two-sided Mann–Whitney test). **o** Confocal images showing NALCN protein expression on the microglial primary process. Scale bar, 2 μm. **p** Quantification of NALCN protein expression on the processes of AISa-MGs vs AISn-MGs (AISa-MG: 0.23 ± 0.01 vs AISn-MG: 0.12 ± 0.01, $n = 4$ mice; two-sided unpaired *t*-test). **q** Representative images of ASAP3 signals on the processes of MGs responding to visual stimulation, before and after injection of the NALCN specific blocker CP96345. Scale bar, 10 μm. **r** Amplitude changes of ASAP3 signals in MGs before and after CP96345 application (Ctrl: 2.85 ± 0.26 vs CP96345: 0.58 ± 0.20; two-sided paired *t*-test. $n = 7$ cells from 4 mice). Whiskers of box plots extend to the 2.5th and 97.5th percentiles of the data. Error bars indicate SEM.

identified some pairs of MGs and PNs with AIS–microglial process interactions and observed that the AIS–microglial process contact was well maintained even after 6 h and 12 h (Supplementary information, Fig. S18f), suggesting that this AIS–MG interaction can exist stably in vivo. The AISa-PNs indeed responded more robustly to visual stimulation compared with nearby AISn-PNs, and this response was suppressed by the THIK-1 specific antagonist C101248 (Fig. 6f–j; Supplementary information, Video S4). As a control, PNs infected with only rAAV-hSyn-AIS-mCherry-WPRE-pA virus did not respond to visual stimulation, and their fluorescence intensity showed little fluctuation (Supplementary information, Fig. S18b). We next performed two-photon imaging on *Cx3cr1-Cre^{ERT};YFP;THIK-1$^{fl/fl}$* (cKO) mice that had been intracranially injected with rAAV-CaMKIIα-NES-jRGECO1α and rAAV-hSyn-AIS-mCherry-WPRE-pA virus 3 weeks earlier, then intraperitoneally injected with tamoxifen for 5 consecutive days before imaging (Fig. 6m). We identified some pairs of MGs and PNs with and without AIS–microglial process interactions (Fig. 6n, o) and found that calcium transients of AISa-PNs responding to visual stimulation were significantly reduced in THIK-1 cKO mice compared with WT mice, whereas calcium transients of AISn-PNs responding to visual stimulation in THIK-1 cKO mice were not obviously affected (Fig. 6p–r; Supplementary information, Video S5), suggesting that THIK-1 cKO in MGs specifically influences calcium responses to visual stimulation in AISa-PNs.

Previous studies have shown that a small population of critical neurons (pattern-completion neurons) within neural ensembles play a crucial role in visual perception.[62,63] Optogenetic activation of a few of these critical neurons (minimum 2 cells) can trigger reactivation of the entire neural ensemble and relevant visual discrimination behavior,[63] suggesting that this small population of critical neurons can regulate the coordinated activity of entire neural ensembles and contribute to cognitive behavior. We therefore examined whether disruption of the small portion of strongly responding AISa-PNs by targeting THIK-1 would influence the coordinated activity of entire neural ensembles. We calculated the neuron synchronicity and connectance indexes of entire neural ensembles responding to visual stimulation (Supplementary information, Fig. S13e) and found that selective THIK-1 inhibition by C101248 in MGs significantly reduced the neuron synchronicity and connectance indexes (Fig. 6k, l). Similarly, THIK-1 cKO in MGs also significantly reduced the neuron synchronicity and connectance indexes of entire neural ensembles (Fig. 6s, t). Together, these results confirm that microglial THIK-1 indeed contributes to the enhanced calcium transient responses of a small portion of PNs that interact with MGs at the AISs, thereby influencing the coordinated activity of entire neural ensembles.

We next tested whether disruption of the functional interaction between AISa-MGs and PNs by targeting THIK-1 would affect visual discrimination behaviors (Fig. 7a). Mice were first trained to perform a Go/No-Go visually guided task in which a vertical drifting grating (the "Go" stimulus) and a horizontal drifting grating (the "No-Go" stimulus) were associated with water reward and no reward, respectively, as described previously.[66] During training, mice gradually learned to lick correctly when Go and No-Go stimuli were randomly presented (Fig. 7b–e); they reached a performance level above 75% on day 4 of training and remained above this level afterward (Fig. 7d). Mice exhibited significantly improved performance, a reduced false-alarm (FA) rate (Fig. 7e), and faster licking onset after 5 days of training (Fig. 7b). On day 6, the performance of mice in the Go/No-Go task was first examined, and the THIK-1 specific antagonist C101248 was then administered into layer 2/3 of V1. The performance of mice in the visual discrimination task was significantly reduced after C101248 application (Fig. 7f, g). Similarly, THIK-1 cKO mice exhibited significantly impaired performance in the visual discrimination task compared with WT mice (Fig. 7j, k). As a control, application of ACSF had no obvious effect on the performance of mice in the visual discrimination task (Fig. 7h, i). Application of the P2Y12R specific antagonist ticagrelor also had no obvious influence on task performance (Supplementary information, Fig. S16d).

Since our data showed that the cell-adhesion molecule ITGB1 is highly enriched in microglial processes associated with neuronal AISs (Fig. 2f, g), we assumed that ITGB1 might mediate the physical interaction between microglial processes and neuronal AISs. We generated *Cx3cr1-Cre^{ERT};YFP;Itgb1$^{fl/fl}$* (*Itgb1* cKO) mice and intraperitoneally injected them with tamoxifen at postnatal day 7 for 5 consecutive days to specifically ablate *Itgb1* from MGs (Fig. 8a, b). *Itgb1* cKO indeed markedly reduced the percentage of AIS–microglial process interactions (Fig. 8c, d). At the same time, *Itgb1* cKO did not change microglial MP or input resistance (Supplementary information, Fig. S19a, b). *Itgb1* cKO also did not alter MG density (Supplementary information, Fig. S19c, d) and only subtly influenced microglial morphology (Supplementary information, Fig. S19e–h). It did not affect excitatory and inhibitory synapse numbers or synaptic transmission (Supplementary

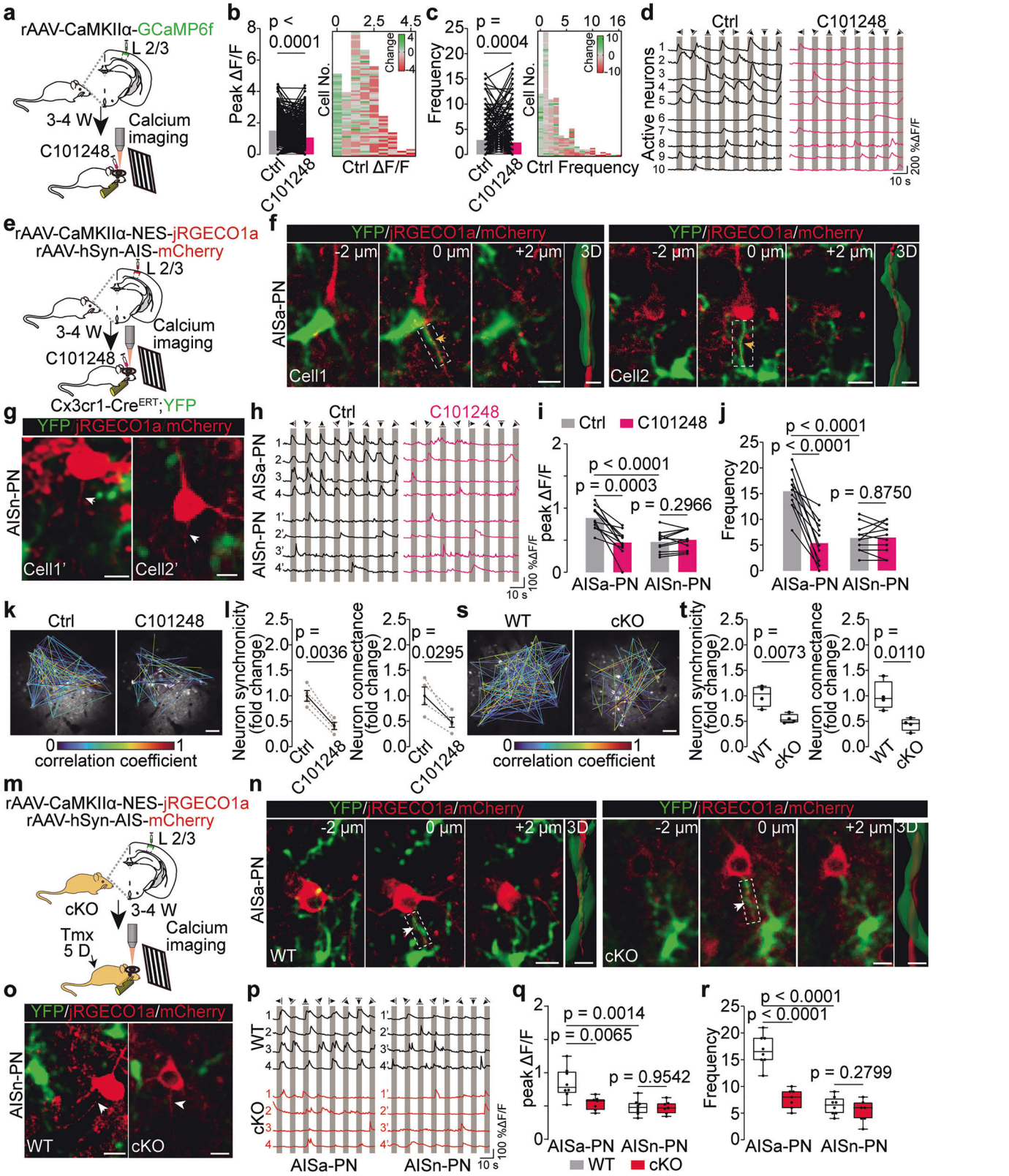

information, Fig. S19i–s). These results suggest that *Itgb1* cKO is a more specific strategy for breaking the physical and functional interaction between neuronal AISs and MGs.

Notably, *Itgb1* cKO resulted in a selective disappearance of strongly responding PNs in the neural ensembles, leading to a significant reduction in the ΔF/F and frequency of calcium transients (Fig. 8e–h). Importantly, *Itgb1* cKO also dramatically reduced the neuron synchronicity and connectance indexes of entire neural ensembles responding to visual stimulation (Fig. 8i, j). We next trained the *Itgb1* cKO mice in the Go/No-Go visually

Fig. 6 Microglial THIK-1 activity specifically regulates the calcium responses of PNs associated with MGs at the AISs. a Schematic of the experimental procedure. **b** Left: plot of peak ΔF/F (Ctrl: 1.52 ± 0.06 vs C101248: 1.18 ± 0.06; $n = 297$ cells from 4 mice; two-sided paired *t*-test). Right: heatmap illustration of changes in peak ΔF/F. **c** Left: plot of the calcium transient frequency (Ctrl: 2.85 ± 0.17 vs C101248: 2.39 ± 0.20; $n = 297$ cells from 4 mice; two-sided Wilcoxon matched-pairs signed-rank test). Right: heatmap illustration of changes in frequency. **d** Samples of the calcium transient traces of PNs in response to visual stimulation. **e** Schematic of the experimental procedure. **f** Representative in vivo two-photon consecutive images and 3D reconstructions showing 2 AISa-PNs. Scale bars, 10 μm and 2 μm. Brown arrows indicate the interactions between the AISs and the microglial processes. **g** Representative in vivo two-photon images showing 2 AISn-PNs. Scale bars, 10 μm. White arrows indicate the neuronal AISs. **h** Samples of calcium transient traces of AISa-PNs and AISn-PNs in response to visual stimulation. **i** Peak ΔF/F values in AISa-PNs (Ctrl: 0.85 ± 0.05 vs C101248: 0.46 ± 0.06; two-sided paired *t*-test. AISa-PN: Ctrl vs AISn-PN: Ctrl, two-sided unpaired *t*-test; $n = 11$ cells from 5 mice) and AISn-PNs (Ctrl: 0.47 ± 0.05 vs C101248: 0.50 ± 0.05; two-sided paired *t*-test; $n = 11$ cells from 5 mice). **j** Frequency of calcium transients in AISa-PNs (Ctrl: 15.73 ± 1.15 vs C101248: 5.46 ± 1.29; two-sided paired *t*-test. AISa-PN: Ctrl vs AISn-PN: Ctrl, two-sided unpaired *t*-test; $n = 11$ cells from 5 mice) and AISn-PNs (Ctrl: 6.36 ± 0.80 vs C101248: 6.46 ± 0.88; two-sided paired *t*-tes; $n = 11$ cells from 5 mice). **k** Example of the neuron synchronicity and connectance of calcium responses among neurons within one neural ensemble. Lines represent edges, and line colors represent correlation coefficients. Scale bars, 50 μm. **l** Neuron synchronicity (left) (Ctrl: 1.00 ± 0.10 vs cKO: 0.41 ± 0.07; $n = 4$ mice; two-sided paired *t*-test) and connectance (right) (Ctrl: 1.00 ± 0.17 vs cKO: 0.48 ± 0.10; $n = 4$ mice; two-sided paired *t*-test) of calcium responses among neurons of neural ensembles. **m** Schematic of the experimental procedure. **n** Representative in vivo two-photon consecutive images and 3D reconstructions showing 2 AISa-PNs. Scale bars, 10 μm and 2 μm. White arrows indicate interactions between AISs and microglial processes. **o** Representative in vivo two-photon images showing 2 AISn-PNs. Scale bars, 10 μm. White arrows indicate neuronal AISs. **p** Samples of calcium transient traces of AISa-PNs and AISn-PNs in response to visual stimulation. **q** Peak ΔF/F values in AISa-PNs (WT: 0.84 ± 0.08 vs cKO: 0.54 ± 0.04; $n = 8$ cells from 4 WT mice; $n = 7$ cells from 4 cKO mice; two-sided unpaired *t*-test; AISa-PN: WT vs AISn-PN: WT, two-sided unpaired *t*-test) and AISn-PNs (WT: 0.48 ± 0.04 vs cKO: 0.48 ± 0.04; $n = 8$ cells from 4 WT mice; $n = 7$ cells from 4 cKO mice; two-sided unpaired *t*-test). **r** Frequency of calcium transients in AISa-PNs (WT: 16.75 ± 1.01 vs cKO: 7.71 ± 0.68; two-sided unpaired *t*-test; $n = 8$ cells from 4 WT mice; $n = 7$ cells from 4 cKO mice; AISa-PN: WT vs AISn-PN: WT, two-sided unpaired *t*-test) and AISn-PNs (WT: 6.38 ± 0.60 vs cKO: 5.29 ± 0.78; two-sided unpaired *t*-test; $n = 8$ cells from 4 WT mice; $n = 7$ cells from 4 cKO mice). **s** Example of the synchronicity and connectance of calcium responses among neurons within one neural ensemble. Lines represent edges, and line colors represent correlation coefficients. Scale bars, 50 μm. **t** Synchronicity (left) (WT: 1.00 ± 0.10 vs cKO: 0.55 ± 0.05; $n = 4$ mice; two-sided unpaired *t*-test) and connectance (right) (WT: 1.00 ± 0.14 vs cKO: 0.44 ± 0.06; $n = 4$ mice; two-sided unpaired *t*-test) of calcium responses among neurons of neural ensembles.

guided behavioral paradigm and found that these mice exhibited significantly impaired performance in the visual discrimination task compared with WT mice (Fig. 8k–n). These results provide direct evidence for the critical roles of the AIS–MG functional interaction in the regulation of neuronal activity and visual perception behavior.

Taken together, our data strongly indicate that the functional interaction between MGs and neuronal AISs can regulate neuronal activity through THIK-1-mediated K^+ release, influencing the coordinated activity of entire neural ensembles and thus contributing to visual discrimination behavior. Our work highlights an important role of the AIS–MG functional interaction in the regulation of neuronal activity and higher-order perceptual functions in the mammalian brain.

DISCUSSION

In this study, we demonstrated the important function of AISa-MG in the regulation of neuronal activity and the coordinated activity of entire neural ensembles, which is important for visual discrimination behavior. Our data suggest that the specific interaction with neuronal AISs gives MGs distinct morphological and transcriptomic characteristics (Figs. 1, 2). Dual whole-cell recording of ex vivo brain slices demonstrated that brief depolarization of MGs can promote the AP firing of PNs that interact with MGs specifically via their AISs but not via their somata or synapses (Fig. 3; Supplementary information, Figs. S5, S6), and this effect relies on K^+ release from MGs through THIK-1 channels (Fig. 4). Importantly, our in vivo two-photon imaging studies revealed that visual stimulation with drifting gratings can induce robust transient depolarizing events specifically on microglial processes through the muscarinic receptors-NALCN axis under physiological conditions (Fig. 5). Brief optogenetic depolarization of MGs can trigger a sub-threshold depolarization restricted to the soma–AIS interfaces of PNs that are associated with MGs through their AISs rather than through their somata (Supplementary information, Fig. S9). Moreover, blockade of microglial THIK-1 function or suppression of microglial depolarizing activity can specifically disturb the calcium responses to visual stimuli of PNs that interact with MGs at AISs (Fig. 6; Supplementary information, Fig. S17) and thereby affect the performance of animals in a visual discrimination task (Fig. 7). Specific disruption of the physical and functional interaction between MGs and AISs had similar effects on neuronal activity and visual discrimination behavior (Fig. 8). Taken together, our results suggest that the direct functional interaction between MGs and neuronal AISs may serve as a fast, flexible, and precise mechanism for modulating neuronal activity, thus contributing to higher-order perceptive and cognitive behaviors (Fig. 8o).

Previous studies have suggested that the functions of MGs, non-excitable immune cells in the CNS, are closely related to changes in their MP. MGs exhibit depolarizing activities under various physiological and pathological conditions.[37–39,67] Microglial depolarizing activities may lead to intracellular K^+ release through outward-rectifying K^+ channels to stabilize the MP, thus providing more driving force for Ca^{2+} entry to activate intracellular signaling pathways.[35,38,68] Interestingly, THIK-1 has been shown to be tonically active in homeostatic MGs, and this is critical for maintenance of resting MP and regulation of microglial ramification and surveillance under physiological conditions.[35] By contrast, Kv1.3 expression and activation can be induced by immune stimuli, which plays important roles in augmentation of pro-inflammatory reactions in numerous inflammation-related brain diseases.[50,69] In this study, THIK-1 channels were more highly distributed on microglial processes that interacted with neuronal AISs, and inhibition or ablation of THIK-1 reversed the facilitation of AP firing by AISa-MG depolarization (Fig. 4). Furthermore, inhibition and ablation of THIK-1 also disturbed the calcium transient responses to visual stimuli of PNs that interacted with MGs at AISs and impaired the coordinated activity of entire neural ensembles, which subsequently affected the performance of awake animals in the visual discrimination task (Figs. 6, 7). These results support the notion that the physiological regulation of neuronal activity and perceptual behaviors by the AISa-MG is dependent on THIK-1 channel activity.

Our data also indicate that sensory input can trigger transient depolarizing activity of MGs, specifically on their processes rather than somata. But how does sensory input trigger transient

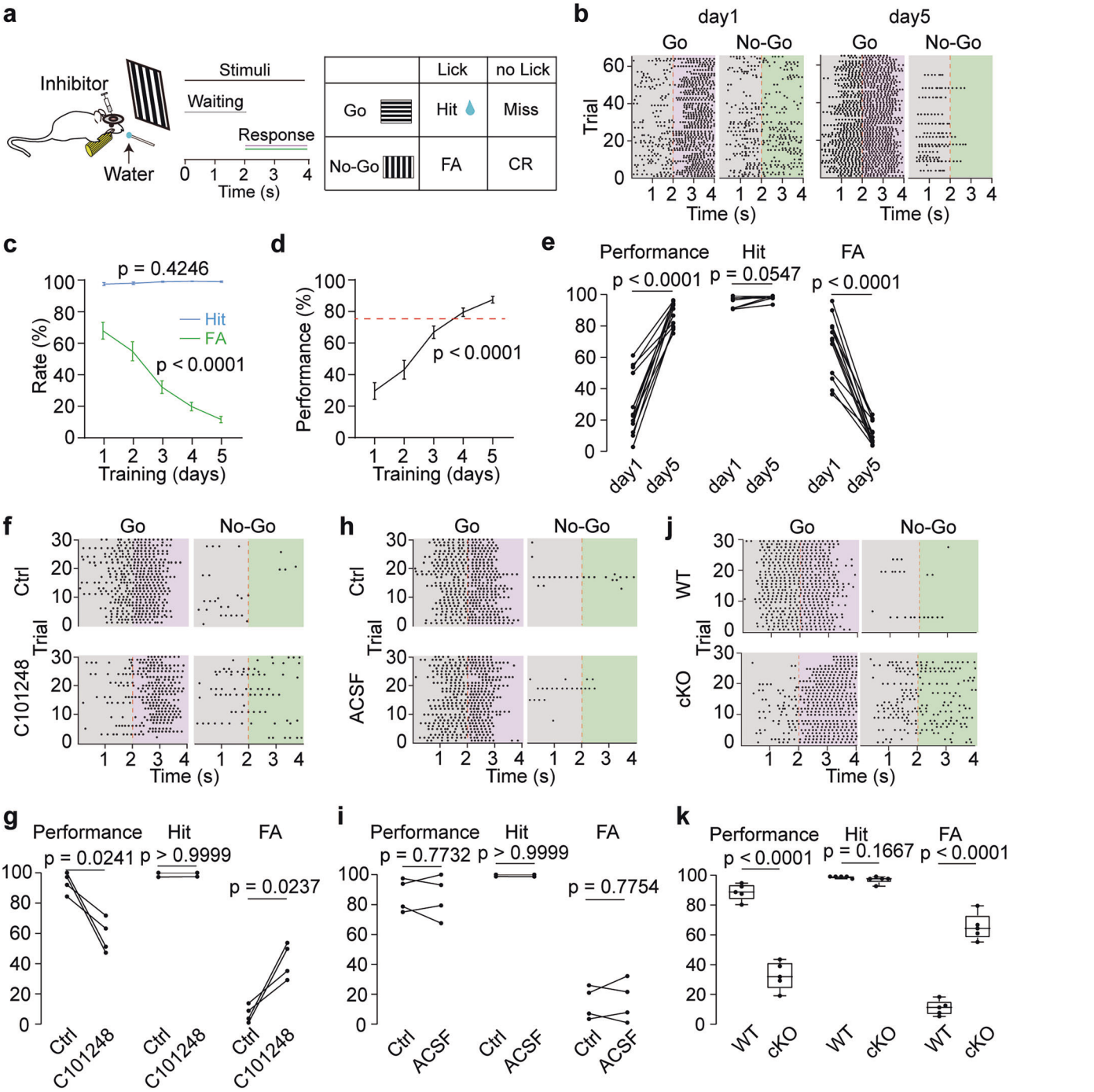

depolarizing activity of MGs? Our results suggest that muscarinic receptors are probably involved, as only their specific antagonist scopolamine blocked the transient depolarizing events in MGs induced by visual stimuli (Fig. 5l, m). MGs express many different GPCRs, such as P2Y12R, muscarinic receptors, and adrenergic receptors.[24,35,36,54] Recent studies have illustrated important roles for these GPCRs in the regulation of microglial functions under various physiological and pathological conditions.[24,35,51–53,55,56] For example, β2-adrenergic receptors were recently reported to regulate MG surveillance during sleep and anesthesia.[51,56,70] Moreover, brain-injury challenge has been shown to activate the purinergic receptor P2Y12R in MGs,[24,35] which gates THIK-1 opening and enhances microglial surveillance.[35] However, our results suggest that under physiological conditions, visual stimuli trigger transient depolarizing activity of MGs selectively through muscarinic receptors but not P2Y12R or adrenergic receptors (Fig. 5; Supplementary information, Fig. S12), suggesting that different GPCRs may play distinct roles in the regulation of different microglial functions. Notably, many previous studies have demonstrated the important functions of muscarinic receptors in visual perception and related behaviors.[58,71] Muscarinic receptors may play critical roles in visual perception in part through MG-mediated modulation of neuronal activity, as shown in our study. Furthermore, one recent study showed that THIK-1 can be activated by both Gi/o- and Gq-Rs-mediated GPCR pathways,[72] indicating that the muscarinic receptor-mediated signaling pathway is likely to activate THIK-1, leading to K^+ release. Indeed, our results showed that after THIK-1 cKO in MGs, the

Fig. 7 Disruption of microglial THIK-1 activation affects visual discrimination behavior. a Schematic of the experimental procedure. FA false alarm, CR correct rejection. **b** Representative examples showing licking behaviors of mice presented with Go and No-Go stimuli on day 1 and day 5 of training. Note that mice exhibited faster licking onset after 5 days of training. Gray boxes indicate the waiting period, purple and green boxes indicate the response period, and dark dots represent licks. **c** Hit rate ($n = 13$ mice) and FA rate ($n = 13$ mice) during 5 days of training. Friedman test for Hit rate and FA rate. **d** Gradually improved performance in the visual discrimination task during 5 days of training ($n = 13$ mice). Note that the performance reached above 75% on day 4 and stayed above this level afterwards. **e** Significantly improved performance in the visual discrimination task after 5 days of training (Performance: day 1: 29.58 ± 5.30 vs day 5: 87.44 ± 2.13; two-sided paired *t*-test. Hit: day 1: 97.48 ± 0.93 vs day 5: 99.06 ± 0.43; two-sided Wilcoxon matched-pairs signed-rank test. FA: day 1: 67.90 ± 5.30 vs day 5: 11.62 ± 1.98; two-sided paired *t*-test). **f** Representative examples showing licking behaviors of mice presented with Go and No-Go stimuli before (Ctrl) and after C101248 administration (C101248). **g** Performance was significantly reduced by C101248 application (Performance: Ctrl: 93.43 ± 3.43 vs C101248: 58.35 ± 5.63; two-sided paired *t*-test. Hit: Ctrl: 99.31 ± 0.69 vs C101248: 99.38 ± 0.63; two-sided Wilcoxon matched-pairs signed-rank test. FA: Ctrl: 5.87 ± 2.84 vs C101248: 41.03 ± 5.84; two-sided paired *t*-test. $n = 4$ mice). **h** Representative examples showing licking behaviors of mice presented with Go and No-Go stimuli before (Ctrl) and after ACSF administration (ACSF). **i** Performance was comparable before and after ACSF application (Performance: Ctrl: 86.28 ± 5.54 vs ACSF: 85.00 ± 7.24; two-sided paired *t*-test. Hit: Ctrl: 99.68 ± 0.32 vs ACSF: 99.67 ± 0.33; two-sided Wilcoxon matched-pairs signed-rank test. FA: Ctrl: 13.41 ± 5.40 vs ACSF: 14.66 ± 6.97; two-sided paired *t*-test. $n = 4$ mice). **j** Representative examples showing licking behaviors of WT and THIK-1 cKO mice presented with Go and No-Go stimuli. **k** Performance was significantly reduced by THIK-1 cKO in MGs (Performance: cKO: 32.53 ± 4.20 vs WT: 88.71 ± 2.47; two-sided unpaired *t*-test. Hit: cKO: 97.86 ± 1.12 vs WT: 99.71 ± 0.29; two-sided Mann–Whitney test. FA: cKO: 65.32 ± 4.04 vs WT: 11.00 ± 2.23; two-sided unpaired *t*-test. $n = 5$ mice). Statistical significance was assessed by two-sided two-way repeated-measures ANOVA for **c** and **d**. Error bars indicate SEM.

microglial transient depolarization induced by visual stimulation did not recover normally to a resting MP level (Fig. 5j, k). This was due to significantly increased membrane resistance (Supplementary information, Fig. S10h) resulting from the lack of tonic THIK-1 conductance, supporting the idea that microglial transient depolarization can drive K^+ release through THIK-1, leading to rapid recovery of the resting MP. Notably, we also found that the Na^+ channel NALCN may directly mediate microglial transient depolarization induced by visual stimulation downstream of muscarinic receptors (Fig. 5n–r), consistent with previous studies that have shown this signaling pathway in other systems.[59,60]

It is well established that extracellular K^+ plays a key role in regulating neuronal excitability; subtle fluctuations in extracellular K^+ concentration have a substantial effect on neuronal MP and also alter the gating of voltage-gated K^+ and Na^+ channels, which collectively influence AP firing.[31,40,73,74] The extracellular K^+ concentration is usually around 3–5 mM; it may briefly rise to 10 mM under physiological conditions and to 10–40 mM under some extreme pathological conditions such as epileptic discharge or spreading depolarization in cerebral ischemia.[31,73] Astrocytes have been suggested to be the main mediator regulating extracellular K^+ homeostasis in the brain through gating of outward- and inward-rectifying K^+ channels.[73,75–79] Interestingly, satellite oligodendrocytes have also been shown to constrain K^+ elevation caused by high-frequency AP firing in the perisomatic neuron domain through gating of some inward-rectifying K^+ channels in neocortical layer 5.[80] In addition to astrocytes and satellite oligodendrocytes, MGs also express many different types of K^+ channels and may participate in the regulation of extracellular K^+. One recent study showed that MGs modulate spreading depolarization during cerebral ischemia, conceivably by interfering with extracellular K^+ homeostasis in the brain.[81] Elevation of extracellular K^+ has long been thought to non-specifically affect the functions of all cell types globally. However, our data suggest that the transient depolarizing activity of AISa-MGs can lead to subtle K^+ release through THIK-1 that may specifically affect the AP firing of associated PNs at a single-cell resolution. Given that the transient depolarizing events occurred specifically on microglial processes (Fig. 5), that THIK-1 channels were highly enriched on microglial processes that interacted with neuronal AISs (Fig. 4l, m), and that tight contact and a narrow extracellular space formed between microglial processes and AISs (Fig. 1h, i), the small amount of K^+ released from AISa-MG processes is likely to be retained in this narrow space and protected from rapid re-uptake by astrocytes and satellite oligodendrocytes, thus fine-tuning the local AIS MP to achieve timely and precise modification of AP firing at the single-cell level. In line with this notion, our data suggest that MG depolarization could give rise to a subtle increase of ~2 mM K^+ in an area immediately adjacent to the microglial processes (Supplementary information, Fig. S8). Moreover, brief depolarization of AISa-MGs, but not AISn-MGs, specifically promoted AP firing of associated PNs (Fig. 3; Supplementary information, Figs. S5, S6) without influencing excitatory and inhibitory synaptic transmission. Mimicking K^+ release by puffing 5 mM K^+ directly onto the AISs of PNs evoked a sub-threshold depolarization and promoted AP firing (Fig. 4f–j). Accordingly, deprivation of microglial intracellular K^+, blockade of THIK-1 opening using its specific antagonist, and ablation of THIK-1 from MGs disrupted the facilitation of AP firing induced by AISa-MG depolarization (Fig. 4).

Previous studies have shown that sensory inputs and perceptual learning can be sparsely coded and driven by small populations of neurons in the sensory cortex.[82–84] It is also well established that ensembles of coactive neurons that likely form preferential synaptic connections with each other[85,86] are the underpinnings of higher-order brain functions such as cognition and behavior.[4,62,63] Interestingly, even a smaller population of critical neurons (pattern-completion neurons) within neural ensembles plays a more crucial role in visual perception,[62,63] and optogenetic activation of a few of these neurons (minimum 2 cells) can trigger reactivation of the neural ensemble and relevant visual discrimination behavior.[63] In line with these previous studies, our data suggest that the physical and functional interaction between MGs and AISs can enhance the calcium responses of associated neurons and influence the coordinated activity of entire neural ensembles, thus contributing to perceptual behaviors (Figs. 6–8). In conclusion, our study identified a new form of functional MG–PN communication whereby the brief depolarizing activity of AISa-MGs can promote neuronal AP firing through THIK-1-mediated K^+ release directly to AISs of associated PNs. This new type of MG–PN communication may play a critical role in higher-order perceptive and cognitive functions in the healthy brain.

MATERIALS AND METHODS

Animal models

All experimental procedures were approved by the Animal Ethics Committee of Southern Medical University in accordance with the National Institutes of Health guidelines for the care and use of experimental animals. C57BL/6 mice were purchased from the Laboratory Animal Center of Southern Medical University, and *Cx3cr1-Cre^{ERT};YFP* mice were kindly provided by Dr. Tian-Ming Gao's lab. TMEM119-Cre^{ERT}, TMEM119-Cre, and ASAP3 reporter mice and *Itgb1$^{fl/fl}$* mice were generated and purchased from Shanghai Model Organisms, and R26-CAG-LSL-2XChETA-tdTomato and Ai40(RCL-ArchT/EGFP)-D knock-in mice were purchased from the

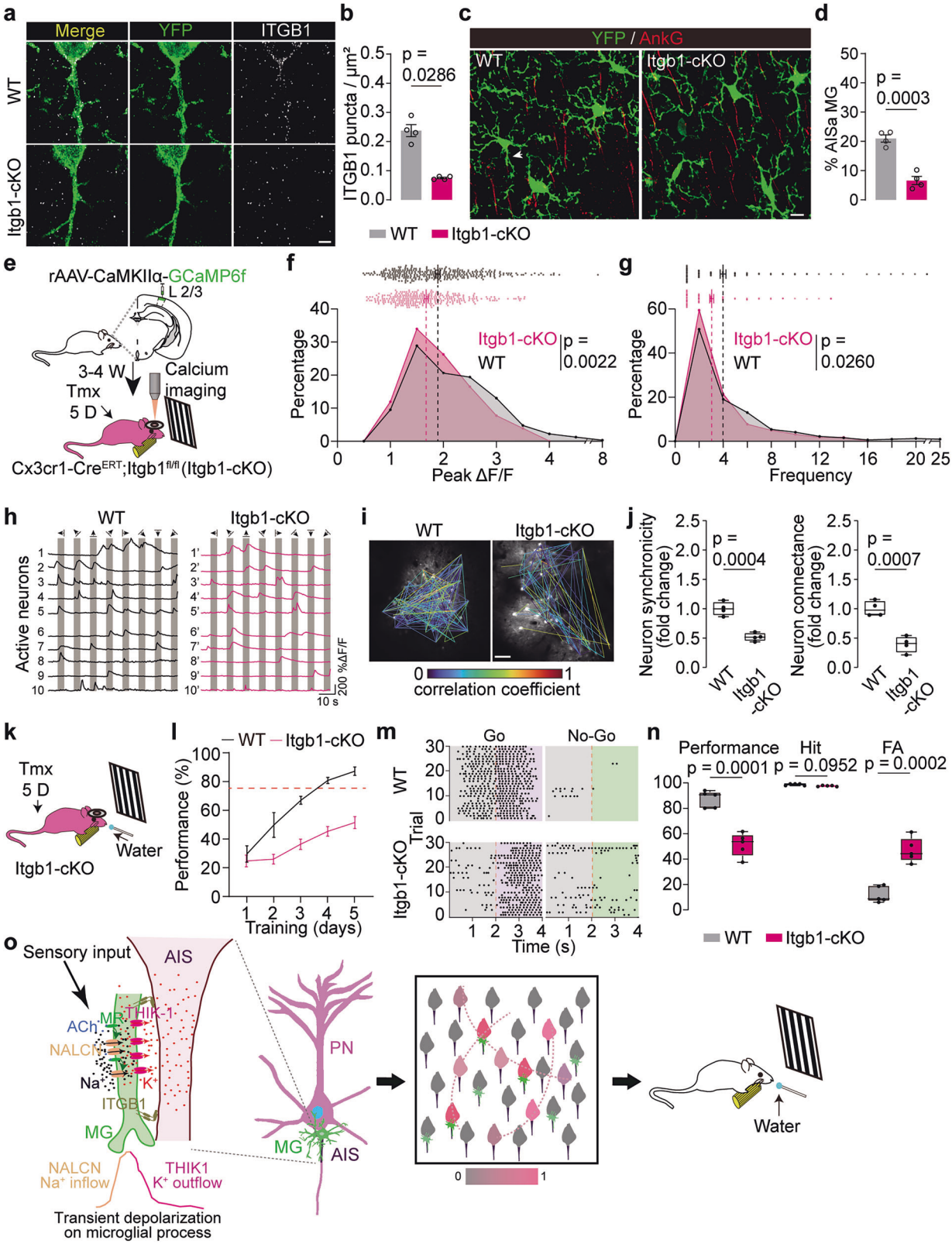

Jackson Laboratory. THIK-1 KO and *THIK-1*$^{fl/fl}$ mice were generated and purchased from GemPharmatech. *Cx3cr1-Cre*^{ERT}*;YFP;Cheta-tdTomato* mice were obtained by crossing *Cx3cr1-Cre*^{ERT}*;YFP* mice with R26-CAG-LSL-2XChETA-tdTomato knock-in mice. *Cx3cr1-Cre*^{ERT}*;YFP;THIK-1* KO, *Cx3cr1-Cre*^{ERT}*;YFP;THIK-1*$^{fl/fl}$ (cKO), and *Cx3cr1-Cre*^{ERT}*;YFP;Itgb1*$^{fl/fl}$ (*Itgb1*-cKO) mice were generated by crossing *Cx3cr1-Cre*^{ERT}*;YFP* mice with THIK-1 KO, *THIK-1*$^{fl/fl}$, and *Itgb1*$^{fl/fl}$ mice, respectively. *Cx3cr1-Cre*^{ERT}*;YFP;Cheta-tdTomato;THIK-1*$^{fl/fl}$ (Cheta;cKO) mice were obtained by crossing cKO mice with R26-CAG-LSL-2XChETA-tdTomato mice. *TMEM119-Cre*^{ERT}*;Cheta-tdTomato* mice were obtained by crossing TMEM119-Cre^{ERT} mice with R26-CAG-LSL-2XChETA-tdTomato knock-in mice. *TMEM119-Cre*^{ERT}*;Ai40D* mice were obtained by crossing TMEM119-Cre^{ERT} mice with Ai40(RCL-ArchT/EGFP)-D knock-in

Fig. 8 ***Itgb1*** **cKO in MGs specifically interrupts the physical and functional interactions between AISa-MGs and PNs and affects visual discrimination behavior. a** Representative images of ITGB1 immunostaining of MGs in V1 of WT vs *Itgb1* cKO mice. Scale bar, 2 μm. **b** ITGB1 expression on microglial processes of WT vs *Itgb1* cKO mice (WT: 0.24 ± 0.02, $n = 4$ mice, vs *Itgb1* cKO: 0.08 ± 0.00, $n = 4$ mice; two-sided Mann–Whitney test). **c** Representative confocal images showing physical interactions between MGs and AISs in WT vs *Itgb1* cKO mice. Scale bar, 10 μm. **d** Percentages of MGs interacting with neuronal AISs (*Itgb1* cKO: 6.61% ± 1.40%, $n = 4$ mice vs WT: 20.98% ± 1.24%, $n = 4$ mice; two-sided unpaired *t*-test). **e** Schematic of the experimental procedure. **f** Peak ΔF/F values (WT: 1.91 ± 0.05 vs *Itgb1* cKO: 1.69 ± 0.04; $n = 315$ cells from 4 WT mice; $n = 286$ cells from 4 cKO mice; two-sided Mann–Whitney test). **g** Calcium transient frequency (WT: 4.02 ± 0.24 vs *Itgb1* cKO: 3.06 ± 0.16; $n = 315$ cells from 4 WT mice; $n = 286$ cells from 4 cKO mice; two-sided Mann–Whitney test). **h** Samples of calcium transient traces of PNs in response to visual stimulation. **i** Example of the synchronicity and connectance of calcium responses among neurons within one neural ensemble. Lines represent connectance, and line colors represent synchronicity. Scale bar, 50 μm. **j** Synchronicity (left) (WT: 1.00 ± 0.06 vs *Itgb1* cKO: 0.52 ± 0.04; $n = 4$ mice; two-sided unpaired *t*-test) and connectance (right) (WT: 1.00 ± 0.07 vs *Itgb1* cKO: 0.39 ± 0.07; $n = 4$ mice; two-sided unpaired *t*-test) of calcium responses among neurons of neural ensembles. **k** Schematic of the experimental procedure. **l** Performance in the visual discrimination task during 5 days of training ($n = 5$ mice). **m** Representative examples showing licking behaviors of WT and *Itgb1* cKO mice presented with Go and No-Go stimuli on day 5 of training. **n** Performance was significantly reduced by *Itgb1* cKO in MGs (Performance: *Itgb1* cKO: 51.43 ± 4.13 vs WT: 87.21 ± 2.93; two-sided unpaired *t*-test. Hit: *Itgb1* cKO: 98.34 ± 0.21 vs WT: 99.46 ± 0.33; two-sided Mann–Whitney test. FA: *Itgb1* cKO: 46.92 ± 4.30 vs WT: 12.25 ± 2.86; two-sided unpaired *t*-test. $n = 5$ mice). **o** Working model: The neuronal AIS and microglial process are physically bound together by the cell adhesion protein ITGB1. Visual stimulation (sensory input) in vivo induces transient depolarization selectively on the process of the AISa-MG interacting with the neuronal AIS through the acetylcholine (ACh)-muscarinic receptor (MR)-Na^+ channel NALCN pathway. Transient depolarization on the AISa-MG process triggers K^+ release through THIK-1 channels directly to the AIS and promotes AP firing of the small portion of associated PNs. This subsequently increases the coordinated activity of the entire neural ensemble, contributing to visual perceptual behaviors. Whiskers of box plots extend to the 2.5th and 97.5th percentiles of the data. Error bars indicate SEM.

mice. *TMEM119-Cre;ASAP3* mice were obtained by crossing TMEM119-Cre mice with ASAP3 reporter mice. *TMEM119-Cre;THIK-1$^{fl/fl}$;ASAP3* (cKO;ASAP3) mice were obtained by crossing *TMEM119-Cre;ASAP3* mice with *THIK-1$^{fl/fl}$* mice. *NG2-Cre^{ERT};THIK-1$^{fl/fl}$* mice were generated by crossing NG2-Cre^{ERT} mice with *THIK-1$^{fl/fl}$* mice. Mice were intraperitoneally injected with 5 μg/g tamoxifen for 5 consecutive days to induce cell type-specific gene knockout. Animals were maintained at the specific pathogen-free animal facilities of Southern Medical University.

Viruses and stereotactic injection

The rAAV2/9-CaMKIIα-GCaMp6f-pA virus was purchased from BrainVTA Biotech. The rAAV2/9-hSyn-AIS-mCherry-WPRE-pA vector was generated from the rAAV2/9-hSyn-mCherry-WPRE-pA vector by fusing the AnkG–Nav1.1 binding sequence to the mCherry sequence, and the virus was produced by BrainVTA Biotech. The rAAV2/9-CaMKIIα-ASAP3-pA and rAAV-CaMKIIα-NES-jRGECO1a viruses were purchased from Brain Case. rAAV2/9-CaMKIIα-GCaMp6f-pA or rAAV2/9-CaMKIIα-ASAP3-pA virus was stereotactically injected into layer 2/3 of the right V1 (2.5 mm lateral and 0.3 mm anterior to lambda, 200–300 μm from the pia surface). rAAV2/9-hSyn-AIS-mCherry-WPRE-pA and rAAV-CaMKIIα-NES-jRGECO1a viruses were injected simultaneously into layer 2/3 of the right V1. In brief, mice were anesthetized by intraperitoneal injection of 0.15–0.25 mL of 20 mg/mL ketamine and 3 mg/mL xylazine in 0.9% NaCl and were then placed in a stereotactic frame. The skull was exposed by a midline scalp incision. A high-speed micro-drill was used to open a small hole in the skull over V1. A glass needle connected to a pico-pump (WPI PV830) was inserted into layer 2/3 of V1, 200 nL of virus was injected over 10 min, and the needle was maintained in place for another 5 min afterward. After injection, the wounds were sutured, and the mice were returned to their home cages. Mice were used for different experiments 3–4 weeks after virus injection.

In utero intraventricular injection

In utero intraventricular injection of rAAV2/9-hSyn-AIS-mCherry-WPRE-pA virus was performed as described previously.[87] In brief, the uterine horns of pregnant *Cx3cr1-Cre^{ERT};YFP* mice at E15–E16 gestation were exposed in a clean environment. AAV virus solution (~1 μL) with 1% fast green (2.5 mg/mL, Sigma) was injected into the embryonic cerebral ventricle with a beveled, sterilized glass capillary (Drummond Scientific, Broomall, PA), followed by lavage of the peritoneal cavity with ~10 mL of warm phosphate-buffered saline (PBS, pH 7.4) containing antibiotics. The uterine horns were replaced, the wounds were sutured, and the mice were returned to their home cages.

Electrophysiology

Acute coronal brain slices were prepared as described previously.[87] In brief, mice were anesthetized and intracardially perfused with an ice-cold cutting solution containing 2 mM KCl, 26 mM $NaHCO_3$, 1.3 mM NaH_2PO_4, 12 mM $MgSO_4$, 0.2 mM $CaCl_2$, and 10 mM D-glucose, pre-bubbled with 95% O_2/5% CO_2 for 10 min. Brains were immediately removed and cut into 350-μm coronal slices using a vibrating blade microtome (Leica Microsystems) in an ice-cold cutting solution bubbled continuously with 95% O_2/5% CO_2. Fresh brain slices were recovered in a chamber with ACSF containing 126 mM NaCl, 3 mM KCl, 1.25 mM NaH_2PO_4, 1 mM $MgSO_4$, 2 mM $CaCl_2$, 26 mM $NaHCO_3$, and 10 mM D-glucose, continuously bubbled with 95% O_2 and 5% CO_2 at 32 °C for 1 h, and then kept at room temperature afterward. Upright fixed-stage microscopes (Nikon Eclipse FN1) equipped with epifluorescence and infrared-differential interference contrast illumination, a camera, and two water immersion lenses (4× and 40×) were used to visualize and locate cells.

To record MGs, whole-cell recordings in voltage-clamp mode were made with patch pipettes containing either an internal solution with potassium (125 mM KCl, 4 mM $MgCl_2$, 1 mM EGTA, 10 mM HEPES, 4 mM Na_2ATP, 0.4 mM Na_3GTP, 10 mM K-phosphocreatine, 1 mM $CaCl_2$, 0.5% fluorescent dye) or an internal solution in which potassium was substituted with cesium (125 mM CsCl, 4 mM $MgCl_2$, 1 mM EGTA, 10 mM HEPES, 4 mM Na_2ATP, 0.4 mM Na_3GTP, 10 mM K-phosphocreatine, 1 mM $CaCl_2$, 0.5% fluorescent dye), with the pH adjusted to 7.25 and the osmolarity adjusted to 305 mOsm/kg. To record PNs, whole-cell recordings in voltage-clamp mode were made with patch pipettes containing 126 mM K-gluconate, 2 mM KCl, 2 mM $MgCl_2$, 0.2 mM EGTA, 10 mM HEPES, 4 mM Na_2ATP, 0.4 mM Na_2GTP, 10 mM K-phosphocreatine, and 0.5% fluorescent dye (pH 7.25 and 305 mOsm/kg). To test whether two cells have direct synaptic connections, 200-ms currents were injected into PNs to induce AP firing or injected into MGs to induce depolarization in current-clamp mode, and postsynaptic voltage responses were recorded in the other cell in current-clamp mode. To assess the functional influence of microglial depolarization on AP firing of PNs, PNs and their AISa-MGs were recorded simultaneously; a 500-ms, 10-pA current was injected into MGs in current-clamp mode, and 500-ms current steps from 0 pA to 150 pA with 10-pA intervals were simultaneously injected into PNs to elicit APs. The Cohen's *d* value was calculated by taking the difference between the mean AP firing number in the current-injection group and the ctrl group, further divided by the standard deviation (SD) of the ctrl group, to reflect the effect size of the increase in AP firing. sEPSCs were recorded by maintaining neurons at −70 mV, and sIPSCs were recorded by maintaining neurons at 0 mV. These data were analyzed using the Mini Analysis program (Synaptosoft).

In another set of recording experiments, *Cx3cr1-Cre^{ERT};Cheta-tdTomato* mice and Cheta;cKO mice were intraperitoneally injected with 5 μg/g tamoxifen for 5 consecutive days before electrophysiological recordings. Microglial depolarization was induced by illumination for 500 ms with 470-nm light, and 500-ms current steps from 0 pA to 150 pA with 10-pA intervals were simultaneously injected into PNs to elicit APs. To specifically inhibit microglial THIK-1 or Kv1.3 potassium channel, 5 μM of the THIK-1 specific inhibitor C101248 (8007, Tocris) or 50 μM of the Kv1.3 specific blocker 5-(4-phenoxybutoxy)psoralen (PAP-1) (HY-10015, MedChemExpress) was added to the internal recording solution for AISa-MGs. To mimic K^+ release to the AIS, a 5-mM K^+ solution was prepared with ACSF and puffed onto the AISs of PNs using glass pipettes (tip resistance, 3.3

mΩ) connected to a pico-pump (WPI, PV830). Alexa Fluor 594 (100 μM) was added to the K^+ solution to visualize the spread of K^+. K^+ puffing (500 ms) was triggered at the same time as 500-ms depolarizing currents were injected into the PNs to elicit APs. To correlate changes in microglial MP with ASAP3 fluorescence signals, various MPs of MGs were manipulated by perfusing ACSF with 3 mM, 15 mM, 30 mM, and 60 mM KCl and determined by whole-cell recording.

The recorded cells were loaded with Alexa Fluor dyes in the internal solution for imaging and identity verification. After recordings, brain slices were fixed overnight with 4% paraformaldehyde (PFA) in PBS (pH 7.4) for subsequent immunohistochemical staining and imaging. All recordings were performed using a HEKA EPC-10 USB (HEKA, Germany) or an Axopatch-700B amplifier (Molecular Devices, USA), and signals were filtered at 2 kHz and digitized at 5–10 kHz. Data were analyzed using FITMASTER (HEKA, Germany) or Clampfit 12 (Molecular Devices, USA).

Recording of K^+ ion dynamics in brain slices

To measure the concentration of K^+ released from the microglial primary process, K^+-sensitive microelectrodes were made as described in previous studies.[40,88] The inner diameter of the glass pipette tip was ~2 μm. The glass pipettes were heated at 200 °C in the presence of 5% dichlorodimethylsilane for 1 h for silanization, then cut to a diameter of ~2–5 μm under a dissecting microscope and backfilled with a solution of 300 mM NaCl and 10 mM HEPES, pH 7.4. The pipettes were primed by immersion in a potassium ionophore cocktail (5% (w/v) valinomycin, 93% (v/v) 1,2-dimethyl-3-nitrobenzene, 2% (w/v) potassium tetrakis(4-chlorophenyl)borate). The primed microelectrodes were then fixed into an electrode holder and connected to the Axopatch 700B recording system. The voltage responsiveness of all microelectrodes was calibrated with standard solutions of ACSF containing various concentrations of KCl (0.1 mM, 1.0 mM, 10 mM, and 100 mM). The pH and osmolarity of the standard solutions were maintained at ~7.25 and ~305 mOsm/kg. The K^+-sensitive microelectrodes were then gently moved onto the microglial primary process in layer 2/3 in the V1 area of acutely prepared brain slices from the *Cx3cr1-Cre^{ERT};YFP*, *Cx3cr1-Cre^{ERT};YFP;Cheta-tdTomato*, or *Cheta;cKO* mouse line. The K^+ voltage responses of MGs to illumination for 500 ms with 470-nm light were measured with or without application of the THIK-1 inhibitor tetrapentylammonium chloride (TPA) (HY-W127637, MedChemExpress) or the specific antagonist C101248 (8007, Tocris). The K^+ voltage responses were also tested upon injection of a 10-pA current into MGs.

RNA-seq

Patch-clamp pipettes with a resistance of 3–4 mΩ were prepared and filled with an internal solution containing RNase inhibitor. MGs were aspirated into the electrodes and swiftly injected into a storage solution. Ten MGs were collected into one tube of the storage solution and were subsequently flash-frozen in liquid nitrogen. MGs were collected within 3 h after slice preparation, as described previously.[35,36] RNA was extracted from the collected MGs and converted into complementary DNA (cDNA) using the Smart-seq2 protocol.[89] The quality of the cDNA was evaluated using an Agilent TapeStation system with High Sensitivity D5000 ScreenTape (Agilent, 5067-5592). The quality of the final cDNA libraries was assessed using a Qubit instrument (Thermo Fisher Scientific) and the Agilent TapeStation. Reads were aligned to the reference genome (Ensembl GRCm38) using HISAT2 v2.2.1. Gene counts were estimated using featureCounts. Statistically significant differences between groups were determined using DESeq2 v1.30.1. Gene expression levels were quantified using rpkmforgenes with uniquely aligned reads.[90] Expression levels were then normalized to the number of reads per kilobase of transcript per million total reads (RPKM values). The RPKM values were $\log_2$-transformed, and all computational analyses were performed in $\log_2$-space. Quantitative analysis and plots of the RNA-seq data were generated using GraphPad Prism software.

Correlative light and scanning electron microscopy

Cx3cr1-Cre^{ERT};YFP mice were used for correlative light and scanning electron microscopy as described in a previous study.[91] Mice were deeply anesthetized and perfused with pre-chilled ACSF, followed by an ice-cold fixative mixture of 4% PFA and 3% sucrose in PBS. The brains were then cut using a Leica VT1200S vibrating blade microtome. These slices were transferred into fresh fixation buffer and post-fixed overnight at 4 °C. After three 5-min rinses in PBS, brain slices were blocked with a glycine blocking buffer (0.1 M PBS, 0.1 M glycine, and 0.05% sodium azide) for 2 h, and then incubated with primary antibodies for 48 h at 4 °C and corresponding secondary antibodies for 2 h at 4 °C. The slices were temporarily mounted on glass slides and imaged with a confocal microscope using a 40×/1.3 NA oil-objective lens; areas of interest were marked by high-power laser scanning in the line mode using LMD6500 (Leica DFC 7000 T). The tissues were then restored in 2.5% glutaraldehyde and 2% PFA. Ultra-thin sections (100 nm) were sectioned with a microtome (Leica EM UC6) and examined with a scanning electron microscope (FEI Helios Nanolab 600i dual-beam SEM) in immersion high-magnification mode (concentric back-scattered detector, 2 kV, 0.69 nA) to acquire the SEM images (back-scattered electron signal).

Surgical procedures for in vivo imaging

In preparation for in vivo imaging, mice were anesthetized and held in a stereotactic frame. A high-speed micro-drill was used to remove a circular window (3 mm in diameter) in the skull over the V1 area (coordinates in mm relative to bregma and midline: 2.9, +2.5) under a dissection microscope. The cranial window was covered by a round glass coverslip (approximately the same size as the circular window) using cyanoacrylate adhesive, and a light circular metal head-plate was mounted on top of the skull with dental acrylic cement. For optogenetic experiments, during head-holder mounting, a small bone flap (~200 μm in diameter) was removed adjacent to the imaging window, and an optic fiber (200 μm in diameter, N.A. 0.37) with a 2.5-mm ferrule stick was implanted into V1 to deliver light. For drug delivery, a cannula was similarly implanted into V1. After surgery, mice were returned to their original cages for recovery. After recovery from surgical anesthesia, mice underwent training to maneuver on the treadmill for 20–30 min for 2 days.

In vivo two-photon calcium imaging and visual stimulation experiments

The head of a recovered mouse was immobilized in a customized head holder mounted with a treadmill by sliding the metal adapter sleeve under screws on the holder, and the mouse moved freely on the treadmill. The head holder and mouse were placed under a lens (25× NA 1.05 XLPlan N objective) of a two-photon microscope with the left eye facing an LED monitor 15 cm away at 45° to the long axis of the animal. Visual stimuli were generated using the Matlab Psychophysics toolbox and presented to the mice on the LED monitor. An Olympus FV1000MPE-RS two-photon microscope equipped with tunable MAITAI eHPDS-OL and InSight DS-OL lasers (Spectra Physics) was used to perform two-channel imaging. The microscope was equipped with a 570-nm dichroic mirror and the following emission filters: 518/45 nm (green channel) and 610/70 nm (red channel). Laser wavelengths of 920 nm and 1120 nm were selected to excite the green and red fluorescence responses, respectively, in all cells within the imaged field of view comprising 50–100 neurons. To record calcium responses to visual stimulation, for each trial, drifting gratings (100% contrast, 2 Hz, 0.04 cycles/°) were presented in 8 directions (0°, 45°, 90°, 135°, 180°, 225°, 270°, 315°) for 4 s on the screen, with a 6-s gray screen interval (5 repetitions). All calcium images were acquired at a frame rate of 2.5 Hz (2 μs pixel dwell time; 256 × 256 pixels in the whole field of view or 800 × 800 in a 180 × 180 μm field of view), short movies (~80 s) were collected at time intervals of 1–2 min, and image acquisition was synchronized with visual stimulation.

To hyperpolarize MGs in the visual stimulation experiment, *TMEM119-Cre^{ERT};Ai40D* mice were used. These mice were intraperitoneally injected with 5 μg/g tamoxifen for 5 consecutive days to induce expression of archaerhodopsin-3 specifically in MGs. Optical activation of archaerhodopsin-3 expressed specifically in the MGs of *TMEM119-Cre^{ERT};Ai40D* mice was induced by a 593-nm yellow light. The light was delivered via an optic fiber (200 μm in diameter) coupled to a laser source and controlled by a stimulator (QAXK-JGQ, Thinkertech, China). The tip of the optic fiber was placed near the superficial layer of V1. To depolarize MGs in layer 2/3, we used a constant laser at a power of 5–8 mW at the fiber tip. The light started at the same time as the drifting gratings were presented and lasted 4 s. Laser-on and laser-off trials were interleaved. For local drug delivery, C101248 (5 μM, 1 μL, dissolved in ACSF; 8007, Tocris) or ticagrelor (200 μM, 1 μL; HY-10064, MedChemExpress) was applied directly to layer 2/3 of V1 through a cannula implanted lateral to the imaging window, and imaging was performed before and 10 min after drug delivery.

Images from in vivo calcium imaging were processed with ImageJ (Fiji) and custom-made programs written in Matlab. All time-lapse images were motion-corrected and referenced to a single template frame using cross-

correlation image alignment (TurboReg plugin for ImageJ v2.1.0). All pixels inside the region of interest (ROI) were averaged to obtain a fluorescence trace for each ROI. Background fluorescence was calculated as the average pixel value per frame from a region without GCaMP expression (blood vessel) and was subtracted from the time-series fluorescence traces to remove interference from background fluorescence. The baseline (F_0) of the fluorescence trace was estimated from the average of inactive portions of the traces (~4 s). The fluorescence change, $\Delta F/F_0$, was calculated as $(F - F_0)/F_0$, with F denoting the fluorescence intensity at any frame. Spikes were inferred from the calcium signals using a threshold of 3 SDs above the noise.

During calcium imaging, neurons exhibited both spontaneous and visual stimulus–evoked calcium responses. We defined the time when the visual stimulation was given as the stimulus-evoked time window. If the initiation points of calcium transients were located within the stimulus-evoked time window, as shown in Supplementary information, Fig. S13d, those calcium transients were taken as visually evoked activities. Only evoked calcium transients were included in the quantification of peak ΔF/F, calcium transient frequency, and neuronal synchronization in response to visual stimulation.

To evaluate the synchronization of neural ensembles' activity, we calculated the correlation coefficients between pairs of neurons by cross-correlation analysis. We shuffled the activity of neurons to random starting points and repeated this process 1000 times to generate surrogate datasets. The significance level was estimated as the correlation coefficient that exceeded 95% of correlation coefficients between these surrogate neuron pairs. Synchronicity was defined as the mean correlation coefficient of all neuron pairs in the ensembles. Connectance was defined as the number of significant edges divided by the maximum possible number of edges in the ensembles.

Primary MG culture, ASAP3 virus infection, and imaging

Primary MGs were obtained from newborn pups of Tmem119-Cre mice. The brain was cut using sterile scissors and digested with digestion solution (Gibco, C25200056). The solution was filtered through a 70-μm-diameter strainer, and the resuspended cells were plated in a flask. After incubation for 12 days, the MGs were collected by shaking at 200 rpm for 2 h and then seeded into confocal dishes. The ASAP3 virus (rAAV-EF1α-DIO-ASAP3-pA, Brain Case) was diluted in the culture medium (1:1000) and incubated for 48 h. ASAP3 signals were acquired using a Nikon ECLIPSE Ni-E confocal microscope with 0.4-Hz time-lapse imaging before and after TPA application.

Primary neuron culture, GCaMp6f virus infection, and imaging

Primary neurons were obtained from E17/18 C57BL/6 mice. The brains were quickly cut using sterile scissors, and the cortices were isolated by carefully removing the meninges. The tissue was digested with 0.25% trypsin and 500 units DNase at 37 °C for 15 min. Digestion was stopped with 10% fetal bovine serum, followed by centrifugation at a low speed. The cells were then resuspended in Neurobasal medium with B-27 (Gibco, 17504044) and GlutaMAX (Gibco, 35050061) and seeded into pre-coated confocal dishes. On day 5, the GCaMp6f virus was diluted in the neuron culture medium (1:5) and incubated for 72 h. Calcium signals were obtained under a two-photon microscope with 2.5-Hz time-lapse imaging before and after application of 20 mM KCl, 10 μM TPA, or 5 μM C101248.

In vivo ASAP3 imaging and photostimulation

To study the influence of MG photostimulation on neuronal MP, we performed two-photon imaging on *TMEM119-Cre^{ERT};Cheta-tdTomato* mice that had been injected with AAV-CaMKIIα-ASAP3 virus. Imaging was performed using an Olympus FV1000MPE-RS two-photon microscope equipped with tunable MAITAI eHPDS-OL and InSight DS-OL lasers (Spectra Physics) and a resonant scanner. Photostimulation was applied using a 940-nm laser via a spiral scan line onto single MGs for 200 ms with a power of 10 mW. ASAP3 signals were acquired using an 860-nm laser immediately after photostimulation. The photostimulation laser and imaging laser were individually controlled by two independent sets of scanning mirrors. Time-series images were acquired at a frame rate of 50 Hz (512 × 150 pixels, 255 μm × 75 μm), and each trial was repeated 3 times.

To study microglial MPs in vivo, two-photon imaging combined with visual stimulation (drifting gratings) was performed in layer 2/3 V1 of *TMEM119-Cre;ASAP3* mice. All images were acquired at a frame rate of 50 Hz (512 × 150 pixels, 255 μm × 75 μm). Visual stimulation was initiated with 4 s of gray screen, followed by 4 s of drifting gratings (100% contrast, 2 Hz, 0.04 cycles/°), and 4 s of gray screen. For local drug delivery, propranolol (10 μM, 1 μL; HY-B0573B, MedChemExpress), scopolamine (2 μM, 1 μL; HY-N0296, MedChemExpress), or ticagrelor (200 μM, 1 μL) was applied directly to layer 2/3 of the V1 cortex through a cannula implanted lateral to the imaging window. All drugs were dissolved in ACSF, and images were obtained before and 10 min after drug delivery.

ASAP3 fluorescence traces of ROIs were acquired using methods similar to those used to obtain calcium traces, and the baseline (F_0) of the fluorescence trace was determined as the average of the upper 25th quartile of the fluorescence intensities across all frames. The fluorescence change, $-\Delta F/F_0$, was calculated as $-(F - F_0)/F_0$, with F denoting the fluorescence intensity at any frame.

Visual discrimination behavior

After the head plate was mounted and the drug-delivery cannula was implanted, mice were returned to their original cages for recovery. Two days later, mice were deprived of water for 1–2 days until they reached 85% of their original weight. On the following 2 days, mice were head-fixed on the treadmill for free maneuvering for 20 min daily. A water reward was delivered by a lick spout that was located 2 mm in front of the tip of the mouse nose and 2 mm below the lower lip. Licks were detected as spout contacts by interruption of an infrared beam. The entire behavioral experiment consisted of three phases: habituation, conditioning, and Go/No-Go visual discrimination.

During the habituation phase (1 day), mice learned to lick from the lick spout to receive a water reward (~4 μL) for each lick. During the conditioning phase (2 days), a vertically oriented grating stimulus (Go stimulus) was presented with 75 trials. Mice were trained to lick in response to the visual stimulus. Each trial started with the 4-s visual stimulus, followed by a 6-s gray interval screen. If a lick was detected during the last 2 s of the visual stimulation (response window), the mouse was rewarded with water. During the Go/No-Go visual discrimination phase (5 days), the Go and No-Go stimuli (vertically and horizontally oriented gratings, respectively) were randomly interleaved. Licking within the response window of a Go trial (Hit) was rewarded with water. For a No-Go trial, licking within the answer period was taken as an FA, and no licking within the answer period was taken as a CR. Neither FAs nor CRs were associated with a water reward. Mice performed the behavioral task in two sessions of 150 trials for 5 consecutive days.

On the day after the 5 days of the Go/No-Go visual discrimination phase, the performance of the mice in the visual discrimination task was assessed before and 10 min after 1 μL C101248, ticagrelor, or ACSF was applied directly to layer 2/3 of the V1 cortex through the cannula.

Hit rate, FA rate, and Performance were calculated as:

Hit rate = number of Hit trials/(number of Hit trials + number of miss trials),

FA rate = number of FA trials/(number of FA trials + number of CR trials),

Performance = Hit rate − FA rate.

Immunostaining and imaging

The recorded brain slices were incubated in a blocking solution (10% normal goat serum and 0.1% Triton X-100 in PBS) for ~2 h at room temperature, and then incubated with primary antibodies, including goat anti-GFP (Novus, NB100-1770, 1:1000), mouse anti-AnkG (NeuroMab, N106/36, 1:500), mouse anti-Beta4-spectrin (NeuroMab, 75-377, 1:500), rabbit anti-Iba1 (Wako, 019-19741, 1:1000), rabbit anti-NeuN (Cell Signaling Technology, 24307S, 1:500), rabbit anti-THIK-1 (Alomone, APC-121, 1:500), rabbit anti-Caspase3 (Cell Signaling Technology, 9661 T, 1:500), mouse anti-Gephyrin (SYSY, 417011, 1:500), rabbit anti-vGAT (SYSY, 131003, 1:500), rabbit anti-Homer1 (Abcam, ab184955, 1:500), mouse anti-vGlut2 (Abcam, ab79157, 1:500), rat anti-MBP (Abcam, ab7349, 1:500), pig anti-Oligo2 (Millipore, ABE1024, 1:500), rabbit anti-ITGB1 (Proteintech, 12594-1-AP, 1:500) and rabbit anti-NALCN (Alomone, ASC-022, 1:500) for 24 h at 4 °C. Brain slices were rinsed 5 times in PBS and incubated with appropriate fluorescence-conjugated secondary antibodies overnight at 4 °C. Fluorescence-conjugated streptavidin (S32351/S11225, 1:1000, Invitrogen) was used to stain neurobiotin-labeled cells. 4′,6-Diamidino-2-phenylindole (DAPI) was used to visualize cell nuclei and identify cortical laminar boundaries. Z-series images were collected using a confocal microscope (Nikon) with 2–5-μm steps, and images were processed and analyzed using Imaris, ImageJ, and Photoshop (Adobe Systems).

Animals for immunostaining were anesthetized and transcardially perfused with cold saline solution and 4% PFA in PBS. Fresh-fixed macaque brain tissues were purchased from Landau Bio, Guangzhou, China. Serial coronal or horizontal sections (~100 μm) were prepared using a freezing microtome (Leica, Germany, CM1950) and processed using procedures similar to those described above for imaging and analysis.

Statistical analysis

Data were analyzed using GraphPad Prism software and expressed as mean ± SEM. Statistical tests used to evaluate significance are shown in figure legends. Details of all statistics used in figures are available from the corresponding author (S.R.) upon reasonable request. Significant differences were defined at $P < 0.05$.

DATA AVAILABILITY

The datasets generated and/or analyzed in this study are provided in Supplementary information, and also available from the corresponding author (S.R.) upon reasonable request.

CODE AVAILABILITY

All custom codes created in Matlab in this study for data acquisition and analysis are available from the corresponding author (S.R.) upon reasonable request.

REFERENCES

1. Saunders, A. et al. Molecular diversity and specializations among the cells of the adult mouse brain. *Cell* **174**, 1015–1030.e16 (2018).
2. Zeisel, A. et al. Molecular architecture of the mouse nervous system. *Cell* **174**, 999–1014.e22 (2018).
3. Harris, K. D. & Mrsic-Flogel, T. D. Cortical connectivity and sensory coding. *Nature* **503**, 51–58 (2013).
4. Yuste, R. From the neuron doctrine to neural networks. *Nat. Rev. Neurosci.* **16**, 487–497 (2015).
5. Jakel, S. & Dimou, L. Glial cells and their function in the adult brain: a journey through the history of their ablation. *Front. Cell Neurosci.* **11**, 24 (2017).
6. Clarke, L. E. & Barres, B. A. Emerging roles of astrocytes in neural circuit development. *Nat. Rev. Neurosci.* **14**, 311–321 (2013).
7. Li, Q. & Barres, B. A. Microglia and macrophages in brain homeostasis and disease. *Nat. Rev. Immunol.* **18**, 225–242 (2018).
8. Nayak, D., Roth, T. L. & McGavern, D. B. Microglia development and function. *Annu. Rev. Immunol.* **32**, 367–402 (2014).
9. Zuchero, J. B. & Barres, B. A. Glia in mammalian development and disease. *Development* **142**, 3805–3809 (2015).
10. Lezmy, J. et al. Astrocyte Ca(2+)-evoked ATP release regulates myelinated axon excitability and conduction speed. *Science* **374**, eabh2858 (2021).
11. Hickman, S., Izzy, S., Sen, P., Morsett, L. & El Khoury, J. Microglia in neurodegeneration. *Nat. Neurosci.* **21**, 1359–1369 (2018).
12. Cserep, C., Posfai, B. & Denes, A. Shaping neuronal fate: Functional heterogeneity of direct microglia-neuron interactions. *Neuron* **109**, 222–240 (2021).
13. Kettenmann, H., Kirchhoff, F. & Verkhratsky, A. Microglia: new roles for the synaptic stripper. *Neuron* **77**, 10–18 (2013).
14. Merlini, M. et al. Microglial Gi-dependent dynamics regulate brain network hyperexcitability. *Nat. Neurosci.* **24**, 19–23 (2021).
15. Jafari, M. et al. Phagocyte-mediated synapse removal in cortical neuroinflammation is promoted by local calcium accumulation. *Nat. Neurosci.* **24**, 355–367 (2021).
16. Schafer, D. P. et al. Microglia sculpt postnatal neural circuits in an activity and complement-dependent manner. *Neuron* **74**, 691–705 (2012).
17. Weinhard, L. et al. Microglia remodel synapses by presynaptic trogocytosis and spine head filopodia induction. *Nat. Commun.* **9**, 1228 (2018).
18. Miyamoto, A. et al. Microglia contact induces synapse formation in developing somatosensory cortex. *Nat. Commun.* **7**, 12540 (2016).
19. Wake, H., Moorhouse, A. J., Miyamoto, A. & Nabekura, J. Microglia: actively surveying and shaping neuronal circuit structure and function. *Trends Neurosci.* **36**, 209–217 (2013).
20. Hong, S. et al. Complement and microglia mediate early synapse loss in Alzheimer mouse models. *Science* **352**, 712–716 (2016).
21. Bartels, T., De Schepper, S. & Hong, S. Microglia modulate neurodegeneration in Alzheimer's and Parkinson's diseases. *Science* **370**, 66–69 (2020).
22. Paolicelli, R. C. et al. Synaptic pruning by microglia is necessary for normal brain development. *Science* **333**, 1456–1458 (2011).
23. Ronzano, R. et al. Microglia-neuron interaction at nodes of Ranvier depends on neuronal activity through potassium release and contributes to remyelination. *Nat. Commun.* **12**, 5219 (2021).
24. Cserep, C. et al. Microglia monitor and protect neuronal function through specialized somatic purinergic junctions. *Science* **367**, 528–537 (2020).
25. Baalman, K. et al. Axon initial segment-associated microglia. *J. Neurosci.* **35**, 2283–2292 (2015).
26. Gallo, N. B., Berisha, A. & Van Aelst, L. Microglia regulate chandelier cell axo-axonic synaptogenesis. *Proc. Natl. Acad. Sci. USA* **119**, e2114476119 (2022).
27. Benusa, S. D. & Lafrenaye, A. D. Microglial process convergence on axonal segments in health and disease. *Neuroimmunol. Neuroinflammation* **7**, 23–39 (2020).
28. Huang, C. Y.-M. & Rasband, M. N. Axon initial segments: structure, function, and disease. *Ann. N. Y. Acad. Sci.* **1420**, 46–61 (2018).
29. Nelson, A. D. & Jenkins, P. M. Axonal membranes and their domains: assembly and function of the axon initial segment and node of Ranvier. *Front. Cell Neurosci.* **11**, 136 (2017).
30. Goethals, S. & Brette, R. Theoretical relation between axon initial segment geometry and excitability. *Elife* **9**, e53432 (2020).
31. Jefferys, J. G. Nonsynaptic modulation of neuronal activity in the brain: electric currents and extracellular ions. *Physiol. Rev.* **75**, 689–723 (1995).
32. McDonough, A. A. & Youn, J. H. Potassium homeostasis: the knowns, the unknowns, and the health benefits. *Physiology* **32**, 100–111 (2017).
33. Wan, Y. et al. Microglial displacement of GABAergic synapses is a protective event during complex febrile seizures. *Cell Rep.* **33**, 108346 (2020).
34. Chen, Z. et al. Microglial displacement of inhibitory synapses provides neuroprotection in the adult brain. *Nat. Commun.* **5**, 4486 (2014).
35. Madry, C. et al. Microglial ramification, surveillance, and interleukin-1beta release are regulated by the two-pore domain K(+) channel THIK-1. *Neuron* **97**, 299–312.e6 (2018).
36. Gyoneva, S. & Traynelis, S. F. Norepinephrine modulates the motility of resting and activated microglia via different adrenergic receptors. *J. Biol. Chem.* **288**, 15291–15302 (2013).
37. Laprell, L., Schulze, C., Brehme, M. L. & Oertner, T. G. The role of microglia membrane potential in chemotaxis. *J. Neuroinflammation* **18**, 21 (2021).
38. Nguyen, H. M. et al. Biophysical basis for Kv1.3 regulation of membrane potential changes induced by P2X4-mediated calcium entry in microglia. *Glia* **68**, 2377–2394 (2020).
39. Wogram, E. et al. Satellite microglia show spontaneous electrical activity that is uncorrelated with activity of the attached neuron. *Eur. J. Neurosci.* **43**, 1523–1534 (2016).
40. Octeau, J. C. et al. Transient, consequential increases in extracellular potassium ions accompany channelrhodopsin2 excitation. *Cell Rep.* **27**, 2249–2261.e7 (2019).
41. Ossola, B. et al. Characterisation of C101248: A novel selective THIK-1 channel inhibitor for the modulation of microglial NLRP3-inflammasome. *Neuropharmacology* **224**, 109330 (2023).
42. Zhang, Y. et al. Purification and characterization of progenitor and mature human astrocytes reveals transcriptional and functional differences with mouse. *Neuron* **89**, 37–53 (2016).
43. Zhang, Y. et al. An RNA-sequencing transcriptome and splicing database of glia, neurons, and vascular cells of the cerebral cortex. *J. Neurosci.* **34**, 11929–11947 (2014).
44. Thornton, M. A. et al. Long-term in vivo three-photon imaging reveals region-specific differences in healthy and regenerative oligodendrogenesis. *Nat. Neurosci.* **27**, 846–861 (2024).
45. Hughes, E. G., Orthmann-Murphy, J. L., Langseth, A. J. & Bergles, D. E. Myelin remodeling through experience-dependent oligodendrogenesis in the adult somatosensory cortex. *Nat. Neurosci.* **21**, 696–706 (2018).
46. Villette, V. et al. Ultrafast two-photon imaging of a high-gain voltage indicator in awake behaving mice. *Cell* **179**, 1590–1608.e23 (2019).
47. Li, B. et al. Two-photon voltage imaging of spontaneous activity from multiple neurons reveals network activity in brain tissue. *iScience* **23**, 101363 (2020).
48. Izquierdo, P., Shiina, H., Hirunpattarasilp, C., Gillis, G. & Attwell, D. Synapse development is regulated by microglial THIK-1 K(+) channels. *Proc. Natl. Acad. Sci. USA* **118**, e2106294118 (2021).
49. Ramesha, S. et al. Unique molecular characteristics and microglial origin of Kv1.3 channel-positive brain myeloid cells in Alzheimer's disease. *Proc. Natl. Acad. Sci. USA* **118**, e2013545118 (2021).
50. Sarkar, S. et al. Kv1.3 modulates neuroinflammation and neurodegeneration in Parkinson's disease. *J. Clin. Invest.* **130**, 4195–4212 (2020).
51. Stowell, R. D. et al. Noradrenergic signaling in the wakeful state inhibits microglial surveillance and synaptic plasticity in the mouse visual cortex. *Nat. Neurosci.* **22**, 1782–1792 (2019).
52. Badimon, A. et al. Negative feedback control of neuronal activity by microglia. *Nature* **586**, 417–423 (2020).

53. Costa, A. et al. Deletion of muscarinic acetylcholine receptor 3 in microglia impacts brain ischemic injury. *Brain Behav. Immun.* **91**, 89–104 (2021).
54. Pannell, M. et al. The subpopulation of microglia expressing functional muscarinic acetylcholine receptors expands in stroke and Alzheimer's disease. *Brain Struct. Funct.* **221**, 1157–1172 (2016).
55. Ma, C. et al. Microglia regulate sleep through calcium-dependent modulation of norepinephrine transmission. *Nat. Neurosci.* **27**, 249–258 (2024).
56. Liu, Y. U. et al. Neuronal network activity controls microglial process surveillance in awake mice via norepinephrine signaling. *Nat. Neurosci.* **22**, 1771–1781 (2019).
57. Gelosa, P. et al. Microglia is a key player in the reduction of stroke damage promoted by the new antithrombotic agent ticagrelor. *J. Cereb. Blood Flow. Metab.* **34**, 979–988 (2014).
58. Gavornik, J. P. & Bear, M. F. Learned spatiotemporal sequence recognition and prediction in primary visual cortex. *Nat. Neurosci.* **17**, 732–737 (2014).
59. Carroll, R. C. & Peralta, E. G. The m3 muscarinic acetylcholine receptor differentially regulates calcium influx and release through modulation of monovalent cation channels. *EMBO J.* **17**, 3036–3044 (1998).
60. Swayne, L. A. et al. The NALCN ion channel is activated by M3 muscarinic receptors in a pancreatic beta-cell line. *EMBO Rep.* **10**, 873–880 (2009).
61. Ferreira, J. J. et al. SLO2.1/NALCN a sodium signaling complex that regulates uterine activity. *iScience* **24**, 103210 (2021).
62. Carrillo-Reid, L., Yang, W., Bando, Y., Peterka, D. S. & Yuste, R. Imprinting and recalling cortical ensembles. *Science* **353**, 691–694 (2016).
63. Carrillo-Reid, L., Han, S., Yang, W., Akrouh, A. & Yuste, R. Controlling visually guided behavior by holographic recalling of cortical ensembles. *Cell* **178**, 447–457.e5 (2019).
64. Polito, A. & Reynolds, R. NG2-expressing cells as oligodendrocyte progenitors in the normal and demyelinated adult central nervous system. *J. Anat.* **207**, 707–716 (2005).
65. Nishiyama, A., Komitova, M., Suzuki, R. & Zhu, X. Polydendrocytes (NG2 cells): multifunctional cells with lineage plasticity. *Nat. Rev. Neurosci.* **10**, 9–22 (2009).
66. Liu, D. et al. Orbitofrontal control of visual cortex gain promotes visual associative learning. *Nat. Commun.* **11**, 2784 (2020).
67. Umpierre, A. D. et al. Microglial calcium signaling is attuned to neuronal activity in awake mice. *Elife* **9**, e56502 (2020).
68. Fomina, A. F., Nguyen, H. M. & Wulff, H. Kv1.3 inhibition attenuates neuroinflammation through disruption of microglial calcium signaling. *Channels* **15**, 67–78 (2021).
69. Di Lucente, J., Nguyen, H. M., Wulff, H., Jin, L. W. & Maezawa, I. The voltage-gated potassium channel Kv1.3 is required for microglial pro-inflammatory activation in vivo. *Glia* **66**, 1881–1895 (2018).
70. Haruwaka, K. et al. Microglia enhance post-anesthesia neuronal activity by shielding inhibitory synapses. *Nat. Neurosci.* **27**, 449–461 (2024).
71. Goard, M. & Dan, Y. Basal forebrain activation enhances cortical coding of natural scenes. *Nat. Neurosci.* **12**, 1444–1449 (2009).
72. Tateyama, M. & Kubo, Y. Regulation of the two-pore domain potassium channel, THIK-1 and THIK-2, by G protein coupled receptors. *PLoS One* **18**, e0284962 (2023).
73. Kofuji, P. & Newman, E. A. Potassium buffering in the central nervous system. *Neuroscience* **129**, 1045–1056 (2004).
74. Malenka, R. C., Kocsis, J. D., Ransom, B. R. & Waxman, S. G. Modulation of parallel fiber excitability by postsynaptically mediated changes in extracellular potassium. *Science* **214**, 339–341 (1981).
75. Bellot-Saez, A., Kekesi, O., Morley, J. W. & Buskila, Y. Astrocytic modulation of neuronal excitability through K(+) spatial buffering. *Neurosci. Biobehav. Rev.* **77**, 87–97 (2017).
76. Kinboshi, M., Ikeda, A. & Ohno, Y. Role of astrocytic inwardly rectifying potassium (Kir) 4.1 channels in epileptogenesis. *Front. Neurol.* **11**, 626658 (2020).
77. Cui, Y. et al. Astroglial Kir4.1 in the lateral habenula drives neuronal bursts in depression. *Nature* **554**, 323–327 (2018).
78. Djukic, B., Casper, K. B., Philpot, B. D., Chin, L. S. & McCarthy, K. D. Conditional knock-out of Kir4.1 leads to glial membrane depolarization, inhibition of potassium and glutamate uptake, and enhanced short-term synaptic potentiation. *J. Neurosci.* **27**, 11354–11365 (2007).
79. Tong, X. et al. Astrocyte Kir4.1 ion channel deficits contribute to neuronal dysfunction in Huntington's disease model mice. *Nat. Neurosci.* **17**, 694–703 (2014).
80. Battefeld, A., Klooster, J. & Kole, M. H. Myelinating satellite oligodendrocytes are integrated in a glial syncytium constraining neuronal high-frequency activity. *Nat. Commun.* **7**, 11298 (2016).
81. Varga, D. P. et al. Microglia alter the threshold of spreading depolarization and related potassium uptake in the mouse brain. *J. Cereb. Blood Flow. Metab.* **40**, S67–S80 (2020).
82. Olshausen, B. A. & Field, D. J. Sparse coding of sensory inputs. *Curr. Opin. Neurobiol.* **14**, 481–487 (2004).
83. Huber, D. et al. Sparse optical microstimulation in barrel cortex drives learned behaviour in freely moving mice. *Nature* **451**, 61–64 (2008).
84. O'Connor, D. H., Peron, S. P., Huber, D. & Svoboda, K. Neural activity in barrel cortex underlying vibrissa-based object localization in mice. *Neuron* **67**, 1048–1061 (2010).
85. Ko, H. et al. Functional specificity of local synaptic connections in neocortical networks. *Nature* **473**, 87–91 (2011).
86. Ko, H. et al. The emergence of functional microcircuits in visual cortex. *Nature* **496**, 96–100 (2013).
87. Ren, S. Q., Li, Z., Lin, S., Bergami, M. & Shi, S. H. Precise long-range microcircuit-to-microcircuit communication connects the frontal and sensory cortices in the mammalian brain. *Neuron* **104**, 385–401.e3 (2019).
88. Octeau, J. C., Faas, G., Mody, I. & Khakh, B. S. Making, testing, and using potassium ion selective microelectrodes in tissue slices of adult brain. *J. Vis. Exp.* **135**, 57511 (2018).
89. Picelli, S. et al. Full-length RNA-seq from single cells using Smart-seq2. *Nat. Protoc.* **9**, 171–181 (2014).
90. Ramskold, D., Wang, E. T., Burge, C. B. & Sandberg, R. An abundance of ubiquitously expressed genes revealed by tissue transcriptome sequence data. *PLoS Comput. Biol.* **5**, e1000598 (2009).
91. Fang, T. et al. Nanobody immunostaining for correlated light and electron microscopy with preservation of ultrastructure. *Nat. Methods* **15**, 1029–1032 (2018).

ACKNOWLEDGEMENTS

We thank Shuji Li, Yingying Fang, Ting Guo, and Xiaowen Li for technical assistance, Dr. Xingmei Zhang and Dr. Rongqing Chen for kindly sharing the habitat space for experimental mice, Dr. Yan Wang and Zhunqiang Zhong for assisting with two-photon imaging, Dr. Bo Peng, Dr. Feng Mei, Dr. Xiang-Dong Sun and Dr. Yue Liu for constructive discussions or comments on the manuscript, and members of the Ren laboratory for valuable input. We are also grateful to Zhongshuang Lv and Xixia Li at the Center for Biological Imaging (CBI), Institute of Biophysics, Chinese Academy of Sciences for helping with electron microscopy sample preparation and scanning. This work was supported by grants from the Noncommunicable Chronic Diseases-National Science and Technology Major Project (2023ZD0507100), the National Natural Science Foundation of China (32270997, 82071268), Guangdong Basic and Applied Basic Research Foundation (2022A1515010219, 2024A1515011338), Guangzhou Science and Technology Plan project (2024B01J1326) and Guangdong-Hong Kong Joint Laboratory for Psychiatric Disorders (2023B1212120004).

AUTHOR CONTRIBUTIONS

S.R., Y.W., and Q.W. conceived the project and designed the experiments; Y.W. performed ex vivo whole-cell recording, imaging, and analyses; Q.W. performed in vivo imaging and analyses; C.G. performed virus injection experiments. S.H. analyzed RNA-seq datasets. Y.W., Q.W., C.G., C.W., J.S., Xinli L., Xiaoli L., and S.F. performed mouse breeding and genotyping. W.Y. assisted with the setup of the recording system. W.W. and T.M.G. helped with experimental design and manuscript improvement. T.M.G. and S.R. acquired fundings and provided resources. S.R., Y.W., and Q.W. wrote the manuscript with input from all other authors.

COMPETING INTERESTS

The authors declare no competing interests.

ADDITIONAL INFORMATION

Supplementary information The online version contains supplementary material available at https://doi.org/10.1038/s41422-026-01218-8.

Correspondence and requests for materials should be addressed to Siqiang Ren.

Reprints and permission information is available at http://www.nature.com/reprints

Publisher's note Springer Nature remains neutral with regard to jurisdictional claims in published maps and institutional affiliations.